IOP Publishing Journal of Physics D: Applied Physics

J. Phys. D: Appl. Phys. **54** (2021) 165201 (19pp) https://doi.org/10.1088/1361-6463/abdb6d

Controlled high temperature stability of microwave plasma synthesized graphene nanosheets

Ondřej Jašek[1], Jozef Toman[1], Dalibor Všianský[2], Jana Jurmanová[1], Miroslav Šnírer[1], Dušan Hemzal[3], Alexander G Bannov[4], Jan Hajzler[5], Pavel St'ahel[1] and Vit Kudrle[1]

[1] Department of Physical Electronics, Faculty of Science, Masaryk University, Brno, Czech Republic
[2] Department of Geological Sciences, Faculty of Science, Masaryk University, Brno, Czech Republic
[3] Department of Condensed Matter Physics, Faculty of Science, Masaryk University, Brno, Czech Republic
[4] Department of Chemistry and Chemical Technology, Novosibirsk State Technical University, 20 K. Marx Ave., Novosibirsk 630073, Russia
[5] Institute of Materials Science, Faculty of Chemistry, Brno University of Technology, Purkyňova 464/118, 61200 Brno, Czech Republic

E-mail: jasek@physics.muni.cz

Received 27 March 2020, revised 29 December 2020
Accepted for publication 13 January 2021
Published 2 February 2021

Abstract

High temperature stability of nanomaterials plays an important role for their application in the field of nanocomposites, batteries, and sensors. Few-layer graphene nanosheets prepared by microwave plasma based decomposition of ethanol exhibited high thermal stability in the oxidation atmosphere in dependence on controlled formation of structural disorder. Analysis of differential thermogravimetry (DTG) curve profile showed three temperature regions, around 345 °C, 570 °C and above 700 °C, related to amorphous phase with a carbon–oxygen functional groups, small defective nanostructures and highly crystalline structure of graphene nanosheets, respectively. Raman spectroscopy and x-ray photoelectron spectroscopy (XPS) analysis of the nanosheets showed an increase of D/G Raman band ratio as well as increasing of sp^3 phase content, from 6.1 at% to 15.2 at%, for highly crystalline and highly disordered structure of the nanosheets. Thermal annealing under synthetic air was used to investigate the variation in D/G and 2D/G Raman band ratio of the samples and to estimate activation energy of oxidation and disintegration process of graphene nanosheets. The highest oxidation resistance exhibited sample with high 2D/G band ratio (1.54) and lowest oxygen content of 1.7 at%. The synthesis process led to stabilization of nanosheet structure by formation of curved edges and elimination of free dangling bonds. The nanosheets prepared in microwave plasma exhibited high surface area, over 350 $m^2\ g^{-1}$, and superior thermal stability with defect activation energy in an oxidation atmosphere higher than 2 eV. Heat release rate during the oxidation process was in correlation with the amount of disorder in the samples. Fast and easy to use technique based on high power Raman spectroscopy was developed for assessment of nanomaterial oxidation resistance.

Supplementary material for this article is available online

Keywords: graphene, microwave plasma, thermal stability, defects, oxidation resistance

(Some figures may appear in color only in the online journal)

1. Introduction

Carbon forms a wide range of different nanostructured materials such as nanocrystalline diamond, fullerenes, carbon nanotubes (CNTs) or graphene. Graphene [1] can be prepared by direct growth on a substrate or in the form of powder depending on application purpose. Graphene in the form of nanopowder can be prepared by mechanical or liquid phase exfoliation [2], laser ablation [3], plasma-based decomposition of organic precursors [4] or high voltage electric discharge plasma of carbon precursors [5]. Freestanding graphene nanosheets, in the form of graphene oxide (GO) or reduced graphene oxide (rGO), are especially useful as filler in composites [6] and anti-corrosive coatings [7], sensing element of gas and chemical sensors [8] or conductor in flexible electronics and transparent displays [9]. Furthermore, the foam-like carbon structures are of high interest in energy storage applications such as supercapacitors and lithium-ion batteries [10]. High temperature stability under inert or oxidation atmosphere plays a key role in these future key enabling technologies applied to electric transport, flexible electronics and smart building and textile materials [11, 12].

Today reduced flammability, i.e. a high thermal stability with low or moderate heat release rate is achieved by insertion of synthetic flame-retardant chemicals into chosen materials. These synthetic flame retardants can be divided into two main categories (a) halogenated [13], such as brominated or chlorinated and (b) non-halogenated [14], where phosphorus-containing chemicals are the main choice. Unfortunately, recent studies in laboratory animals and humans have linked the most widely used flame retardants to increased risk of cancer, memory loss, learning disability and fertility problems [15]. At the same time, these chemicals cause widespread contamination of water resources and natural wildlife habitats [15–17]. It is therefore of the utmost importance to develop new environmentally friendly and biocompatible materials with high temperature thermal stability and controllable heat release characteristics.

Among others, two main groups of synthesis methods of graphene nanopowder are: (a) high temperature decomposition of organic precursors [4] and (b) liquid exfoliation of graphite crystals into the form of GO and its consecutive reduction [18]. Other methods based on separation of individual graphene layers from graphite flakes are based on ultrasonication, intercalation, shear forces or microwave (MW) irradiation [19]. Liquid exfoliation belongs to the most frequently used technique for preparation of GO and rGO nanoflakes [20]. The preparation process involves three steps: dispersion in a solvent, exfoliation procedure and purification step. During the preparation, the graphite source and graphene based output material are exposed to a number of chemicals (acids, salts, reduction compounds) and processing steps which leave the structure contaminated by other elements and are very time consuming. To avoid these elaborate procedures, an alternative bottom-up method to liquid exfoliation technique was developed in a form of graphene nanosheets synthesis based on MW plasma decomposition of organic precursors at atmospheric pressure.

Gas phase synthesis of graphene (GSG) nanosheets by decomposition of ethanol in MW discharges represents a simple single-step method without need of any reprocessing (reduction, cleaning) of prepared product. It is an environmentally friendly method of producing high quality graphene nanosheets with low oxygen content and low amount of defects. Plasma environment can be also used for surface modification by nitrogen or oxygen related species and for further functionalization of carbon based nanomaterials [21]. It was also recently shown that graphene nanopowder prepared by such a technique is biocompatible [22, 23]. This method was first published by Dato *et al* [24] and further investigated by Tatarova *et al* [25] and a model of the synthesis process was developed by Tsyganov *et al* [26]. Zhong and Hong [27] described recently use of gliding arc discharge in $Ar/CH_4/H_2$ mixture for synthesis of graphene nanosheets and showed how concentration of carbon species influences formation of carbon cluster and how the presence of C–H bonds reduces dangling bonds on carbon cluster edges.

In general, thermal stability of carbon materials depends on their structure and amount of defects. Defects in graphite and diamond significantly contribute to a decrease in the oxidative stability of these materials. These defects include dislocations and vacancies in the crystal structure, edges, steps and dangling bonds on the crystal facets and are particularly reactive with oxygen at high temperatures. Elimination of these defects by annealing at higher temperatures can improve their crystallinity and enhance their thermal stability [28]. Thermogravimetry analysis (TGA) analysis of carbon materials in an oxygen-containing atmosphere showed that their thermal stability depends on allotrope structure and Cruptom *et al* [29] reported maximum weight loss for C_{60}, diamond, and graphite at 600 °C, 710 °C and 850 °C, respectively. In case of a good quality graphene nanosheets most of the weight loss occurs above 580 °C which is comparable to multi-walled CNTs (650 °C) [28] and liquid phase exfoliated few layer graphene (600 °C) [30]. As can be seen oxygen significantly limits the thermal stability of carbon allotropes and above 800 °C anaerobic atmosphere is required.

In this work we show that graphene nanosheets synthesized using dual channel microwave plasma torch (MPT) at atmospheric pressure by decomposition of ethanol possess superior thermal stability in comparison to rGO nanoplatelets and that it is possible to distinguish structures with different amount of disorder from characteristics of differential thermogravimetry (DTG) curve and its heat release rate.

2. Material and methods

2.1. Synthesis of graphene nanosheets using dual-channel MPT

Gas phase synthesis of graphene nanosheets was carried out by decomposition of ethanol in dual channel MPT (figure S1 (available online at stacks.iop.org/JPD/54/165201/mmedia)). The experimental apparatus consisted of a MW generator, working at frequency of 2.45 GHz, 2 kW maximum power P_{MW}, connected to a standard rectangular waveguide and

transmitting the MW power through a coaxial line to a nozzle electrode enclosed in the quartz tube reactor. Ferrite circulator protected the generator from the reflected power by rerouting it to the water load. Matching of the plasma load to the line impedance was achieved by a three-stub tuner. The gases were supplied to the discharge chamber through the carbon nozzle electrode which had two gas channels. The central channel (0.8 mm diameter), in the nozzle axis, was used for introduction of working gas—argon Q_C and subsequent ignition of plasma. The secondary channel (annulus with outer radius 8.4 mm and inner radius 7.7 mm) was used for introduction of carrier gas—argon Q_S with ethanol precursor vapors into the plasma environment. Carrier gas has flown through a temperature stabilized bubbler with ethanol before entering the secondary gas channel. The gas flows were controlled by Bronkhorst electronic flow controllers. Reactor chamber consists of a 20 cm long quartz tube with 8 cm diameter. The quartz tube is terminated by aluminum flanges and sealed from the outside environment by nitrile butadiene rubber o-rings and elastic silicone gaskets. The discharge was ignited in the central channel argon flow and the precursor was added to the discharge through secondary channel and discharge was stabilized. Deposition time was 5 min and after the deposition the reactor was cooled down under Ar atmosphere. Synthesized nanopowder was collected from the reactor wall or Si/SiO_2 substrate fixed in the holder above the discharge and further analyzed. More details about experimental setup and procedure can be found in our previous publications [31, 32].

We have shown recently, that modification of deposition conditions in dual-channel MPT discharge leads to controlled synthesis of carbon nanomaterials with different amount of sp^2/sp^3 bond ratio, D/G band ratio, defectivity and morphology as discussed in detail in [31, 32]. These properties have a direct influence on functional properties of graphene nanosheets. On the basis of the selected properties, three samples were synthesized for the thermal stability study. High quality GSG nanosheets (G) and GSG nanosheets with low amount of disorder (ldG) were prepared at 350 W of delivered MW power in laminar and turbulent gas dynamics mode, respectively. Highly defective GSG nanosheets with high amount of disorder (hdG) were synthesized at lower power of 210 W and turbulent gas flow dynamics. In all cases the liquid mass flow rate of ethanol was 45 mg min^{-1} and argon secondary gas channel Qs was 700 sccm. The central channel gas flow dynamics was changed by variation of flow rate between 360 and 920 sccm.

2.2. rGO preparation method

High purity artificial graphite was sieved using sieve with a mesh size of 100 μm. Then, 20 g of graphite was placed into the flask with 460 ml of concentrated H_2SO_4 (95.6%) and 10 g of solid $NaNO_3$. The resulting mixture was mixed by the magnetic stirrer for 10 min and kept at the temperature of 0 °C in an ice bath. After 15 min, anhydrous $KMnO_4$ (60 g) was added to the mixture of graphite/H_2SO_4/$NaNO_3$ and the resulting mixture was kept for 20 min at 0 °C followed by the heating to 35 °C for 30 min. To perform the hydrolysis of graphite intercalation compounds, the mixture was poured into the flask with 920 g of ice and kept at the room temperature (25 ± 2 °C) for 15 min. The last stage of synthesis was the addition of 840 ml of H_2O_2 (hydrogen peroxide content in reagent was 32%) and the mixture was kept for an additional 15 min at the room temperature. The prepared GO was washed by deionized water and dried in air at 90 °C for 24 h.

The prepared GO was reduced by thermal exfoliation (reduction) technique. The sample (2 g) was placed in a hermetically sealed steel vessel (volume was 150 ml). The vessel was put in the furnace and was heated from room temperature (25 ± 1 °C) to 350 °C at a rate of 15 °C min^{-1}, after reaching 350 °C the sample was kept at constant temperature for 55 min. Such prepared powder was further sonicated in an ultrasonic bath UZV-200 (22 kHz) in isopropanol using specific power of 1.45 W cm^{-3} for 12 h to obtain clean rGO material. The cycle of treatment was 20 min sonication +5 min break (for cooling down the bath) and 5 min for changing the cooling water. Total time of treatment was 12 h.

2.3. Material characterization

Samples were imaged by scanning electron microscopy (SEM) with TESCAN MIRA3 microscope with Schottky field emission electron gun equipped with secondary electron (SE) and back-scattered electron (BSE) detectors as well as Oxford Instruments Energy-dispersive x-ray (EDX) analyzer. Transmission electron microscopy (TEM) was carried out using MIRA3 scanning TEM (STEM) mode and FEI Tecai F20 microscope. Image analysis (determination of nanosheet size and inter-layer distance, Fast Fourier transform (FFT) analysis) was carried out using ImageJ Fiji software.

Thermogravimetric analysis and differential scanning calorimetry (DSC) were carried out using a Setaram Setsys Evolution 1750 instrument. The analyses were conducted in a dynamic air atmosphere (20 $sccm^{-1}$) with a constant heating rate of 10 °C min^{-1} in the temperature range from 40 °C to 1000 °C. For comparison purposes, one experiment was carried out with a constant heating rate of 2 °C min^{-1}. The obtained data were processed using the Setaram Processing software.

The phase composition and crystallite size was studied by powder x-ray diffraction (XRD) on a PANalytical X'Pert Pro MPD device using Co radiation ($\lambda_{K\alpha 1}$ = 0.178901 nm) at reflection Bragg-Brentano geometry. The tube power was at 40 kV and 30 mA. Angular range: 5°–90° 2θ, step size: 0.03, time pre step: 100 s, the total scan time: 2166 s. Fixed divergence slit of 0.5° was used. The samples were placed on a zero-background silicon wafer. The data were processed with the help of the Panalytical HighScore 4.8 plus software and JCPD PDF 2 database.

XPS analysis was performed using ESCALAB 250Xi (Thermo Scientific, UK) x-ray photoelectron spectrometer equipped with a conventional hemispherical analyser. Monochromatized Al K_α (1486.6 eV) x-ray source was focused into elliptical spot size at 650 μm. The Lorentzian line profile natural broadening of Al K_α was approximately 0.02 eV and full instrumental broadening, characterized by Gaussian

line profile, including thermal effects was 0.2 eV as determined by fitting Fermi energy, 0 eV, line profile. The pass energies were set to 50 eV for wide-scan and 20 eV for high-resolution elemental scans, respectively. These pass energies correspond to energy resolutions of 1.0 and 0.1 eV, respectively. Charge compensation was performed with a self-compensating device using field emitted low energy electrons. Measurements were performed under ultra-high vacuum 10^{-6} Pa and room temperature.

Raman spectroscopy was carried out using the HORIBA LabRAM HR Evolution system with 532 nm laser, 100× objective, 5% ND filter (500 mW maximum power), 600 mm^{-1} grating and 30 s acquisition time in the range from 1000 to 3200 cm^{-1}.

NOVA 2200e high-speed gas sorption analyzer (Quantachrome Instruments) was used to determine the specific surface area. The samples were weighed into a measuring cell (0.005 g). The measuring cell was placed in a degassing station where the degassing process was carried out at 300 °C for 70 h. After cooling, the samples were placed in a measuring station. The measurement parameters were set as follows: thermal delay—1 200 s, pressure tolerance—6.6 Pa, equilibration time—90 s. The adsorption and desorption isotherms were measured under the conditions of liquid nitrogen (−196 °C) from 0.05 to 0.95 of relative pressure P/P_0. Obtained data were processed by NovaWin software and specific surface area was calculated by the method of multi-point Brunauer–Emmett–Teller (BET) from seven valid points.

The thermal stability study under various gas atmospheres was carried out by samples annealing in quartz glass tube (1000 long, inner diameter 45 mm) placed in the center of cylindrical horizontal furnace Classic 5011T with 400 mm length and hot zone length of 150 mm terminated with KF flanges. The temperature inside the furnace was measured by the type S thermocouple and controlled by Claire electronic control unit. The gas flow rates were controlled by Bronkhorst electronic flow meters and the whole system was evacuated by a turbomolecular pump. The graphene nanosheets powder was put into a quartz boat and placed in the middle of the furnace. The annealing was done in the following sequence. The whole experimental setup was flushed by Ar flow (2.5 lpm) for 5 min to avoid the air impurities during the annealing. The sample was heated to its target temperature (350 °C–750 °C, 10 °C min^{-1}) under synthetic air N_2/O_2 (800/200 sccm) and in ambient air (RH 65%). The sample was then rapidly cooled down by shifting the oven with regard to sample position by 300 mm and cooled down under Ar flow (1000 sccm) to the room temperature.

3. Results and discussion

3.1. SEM and TEM characterization of nanomaterial

All types of samples were analyzed by SEM and showed substantial structural differences between MW plasma synthesized graphene nanosheets and GO samples.

The bottom-up approach of GSG synthesis resulted in foam-like ordering of individual graphene nanosheets with curved edges and thickness of several nanometers (figures 1(a)–(c)). The nanosheets were rectangular in shape and hundreds of nanometers in size. No impurities were found in the structure of the deposit and no large particles originating from erosion of carbon nozzle were found in the nanopowder. While the deposition led to synthesis of nanosheets with targeted amount of defects it was very difficult to observe any unambiguous difference in their SEM images.

On the other hand, the rGO powder (figure 1(d)) consisted of a mix of nano palettes and exfoliated graphite flakes with size ranging from several μms to hundreds of μms with fine edge structure. Due to the way the rGO sample was prepared, it is expected to be contaminated with chemical substances used in the preparation process. Sample contamination was detected by imaging with the BSE detector in SEM, where bright areas represented heavier elements. Precise chemical analysis of rGO was performed using an EDX analyzer. The rGO sample contained 1.5 at% of contamination, mainly S 0.4 at%, K 0.2 at% and Mn 0.2 at%. The carbon and oxygen in rGO sample was 90:10 at% ratio and was consistent with the result of XPS analysis.

GSG nanosheets were analyzed by high resolution transmission electron microscopy (HRTEM) (figure 2). The size determined by TEM was in agreement with SEM results and the number of layers in the nanosheets structure varied from 2 to 10, with interlayer distance of 0.34 nm. The curved and overlapping nanosheets' edges could be observed as well. FFT image analysis of G sample image (figure 2(a)) exhibited six-fold symmetry of a few-layer structure (top left) as well as overlaid edge of twisted bilayer graphene (middle section), in agreement with results of Limbu *et al* [33]. The curved and closed edges are the consequence of a stabilization process to minimize energy of nanosheet structure by elimination of high energy dangling bonds on its edges [34]. The corrugations, edges and topological defects caused the relatively high intensity of D band in our samples in comparison with CVD grown graphene. The hdG sample exhibited more disorder and the few-layer structure was overlaid with small fragments of incomplete additional layers on its surface as can be seen in figure 2(c). One can notice smooth edges of the nanosheet structure which correspond to curved, closed structure as reported by Liu *et al* [35]. The observation of defective parts of the nanosheets are in agreement with TEM analysis of GSG nanosheets by Dato and Frenklach [36]. Reduced graphite oxide sample was generally too thick to carry out effective HRTEM analysis and global STEM analysis (figure 2(d)) was used instead.

3.2. XRD analysis

Bragg-Brentano technique in the interval from 5° to 90° 2θ angle was used for material characterization. Strong graphite (002) (JCPDS 75-1621) diffraction at 30.1° (0.335 nm) could be observed in all samples, but this peak appeared to be slightly shifted to lower angle values i.e. higher interlayer distances, in GSG samples (figure 3). Weaker graphite diffraction peaks (100), (101) and (004) could be observed in rGO sample as well. Neither rGO nor GSG samples diffraction pattern

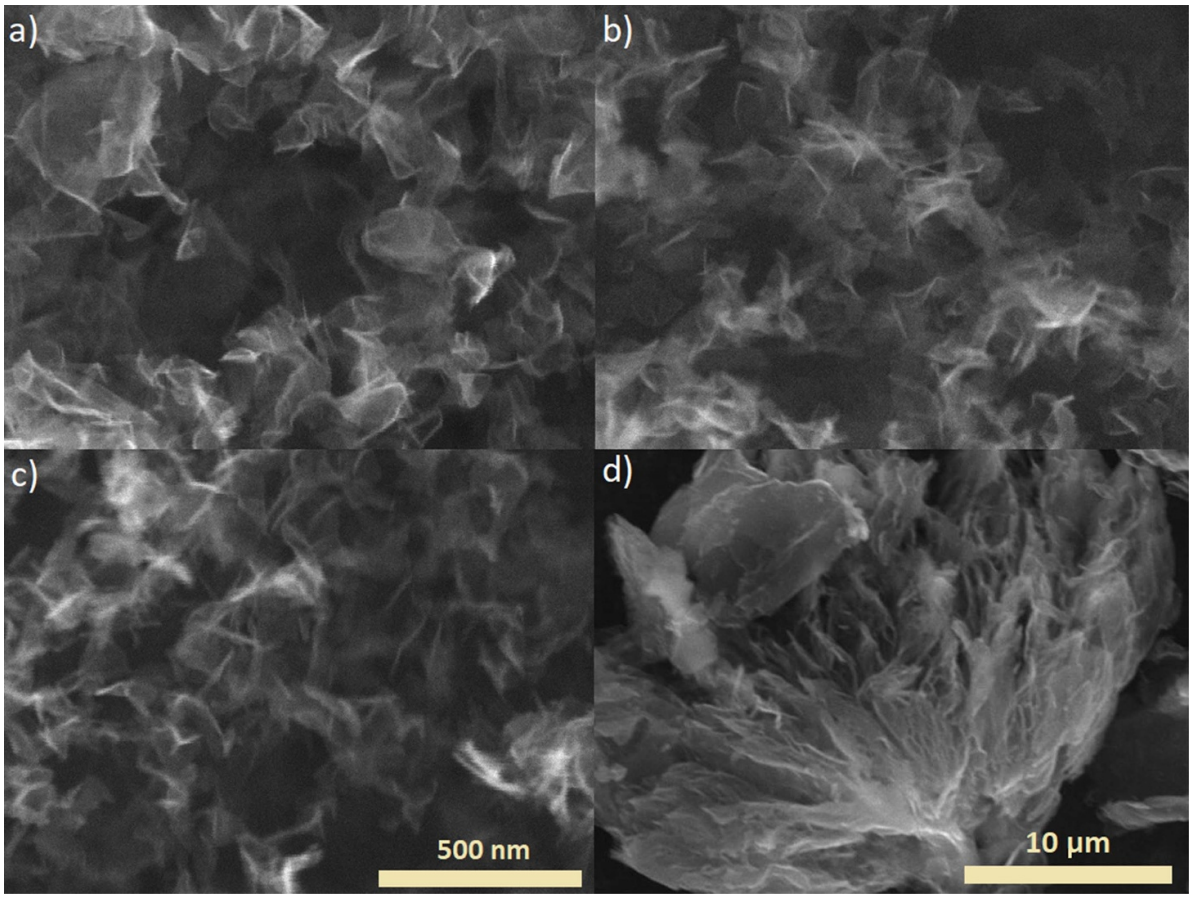

Figure 1. Secondary electron SEM images of GSG nanosheets and reduced graphene oxide: (a) G, (b) ldG, and (c) hdG and (d) rGO sample, respectively. (a)–(c) At the same scale indicated by the scale bar.

exhibited peak at 13.4° (0.855 nm) assigned to intercalated graphite (JCPDS 04-0221) structure of graphite oxide [37]. Neither rGO nor MW plasma graphene nanosheets samples diffraction pattern exhibited this XRD peak. The crystallite size determined from Scherrer formula was approximately 4.6 nm and 21.7 nm for GSG nanosheets and rGO sample, respectively.

3.3. Raman spectroscopy analysis

Raman spectroscopy is a well-established technique for analysis of carbon based nanomaterial structural properties [38]. The normalized intensities of Raman bands and their full width at half maxima (FWHM) values could be used as a fingerprint of structural network disorder and were used for quantification of various structural imperfections for graphene by Ferrari *et al* [39], GO by Pimenta *et al* [40], carbon black by Pawlyta *et al* [41] and amorphous carbon by Sadezky *et al* [42]. First and second-order Raman vibrational modes of carbon related materials were found in the analyzed range (1000–3200 cm^{-1}) of the measured Raman spectra. The first-order region consisted of five spectral bands, four disorder and defects related bands (D^*—1210 cm^{-1}, D—1348 cm^{-1}, D^{**}—1500 cm^{-1} and D′—1620 cm^{-1}) and 'graphite' G band, E_{2g} vibrational mode, at ∼1580 cm^{-1}. The G band was found in the Raman spectra of graphite related samples due to the in-plane bond stretching of carbon atoms in crystal structure with sp^2 hybridization. The second-order region could be deconvoluted into three bands (G^*—2450 cm^{-1}, 2D—2690 cm^{-1} and D + G—2950 cm^{-1}). The origin of the higher-order bands, i.e. G^* is, according to the literature [43], clearly a second overtone of the D^* and D bands. The origin of the Raman signal at 2950 cm^{-1} is not clear and still under debate [44], although it is usually denoted as D + G band. For appropriate analysis of the samples, fitting of the 2D band with Lorentz peak was performed and its intensity normalized to the G band intensity could be used, together with FWHM value, to quantify the number of graphene layers of graphene nanosheets [39]. 2D/G band ratio is used to differentiate between single and few-layer graphene structures in graphene samples with 2D band being independent of defects and activated by an excitation of two phonons from the transverse optical (TO) branch. This behavior is strongly enhanced in single layer graphene.

However, in our study, we observed two distinct extremes. 2D band intensity was either very low in case of rGO sample or high, approximately of the same intensity, for all GSG samples. Each of the studied samples showed characteristic Raman spectra.

Raman spectra on figure 4(a) correspond to well graphitized GSG nanosheets (G) with low defect density as can be derived from the relatively intensive 2D band and low,

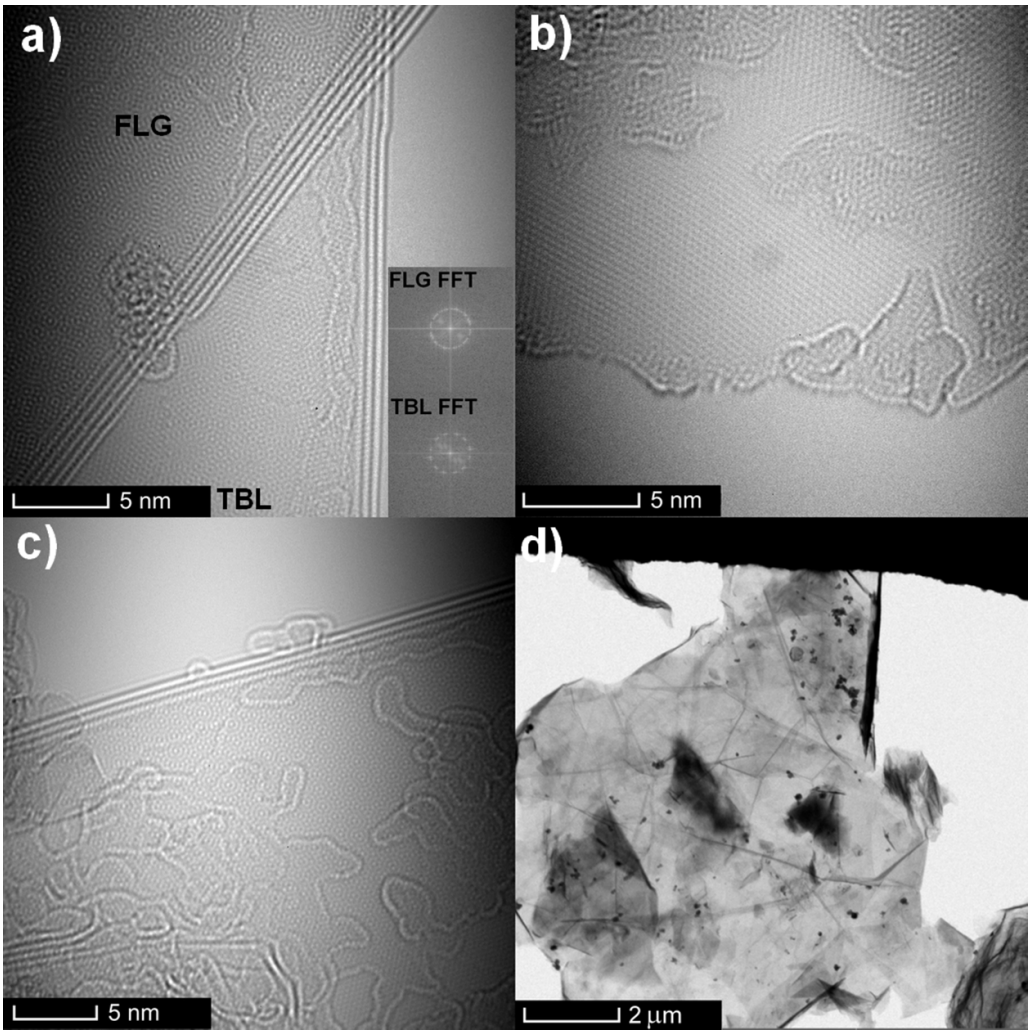

Figure 2. TEM analysis of (a) G, (b) ldG and (c) hdG GSG samples, (d) STEM image of rGO flake. Inset—FFT analysis of few-layer graphene (FLG) and twisted bi-layer (TBL) part of the nanosheets.

well defined D peak. Changing the deposition conditions slightly out of synergy between absorbed MW power and residence time of carbon species in the assembly zone of plasma flame, as described in previous work [31], formed turbulent gas dynamics and the resulting nanomaterial showed higher defectivity and more disordered structure which was reflected in its Raman spectra (figure 4(b)). Raman spectra of defective graphene nanosheets (ldG) showed an increased intensity in the D band region which led to an increase of D/G bad ratio from 0.64 to 1.05. This region was now fitted with two additional defect-activated bands (D^* and D^{**}) around the D band region. Lowering the delivered MW power led to synthesis of even more defective nanostructures (hdG) as seen in figure 4(c). The intensity of the defect-activated 'shoulder' bands (D^*, D^{**} and D') further increased, representing a more disordered structure and a presence of a higher amount of amorphous phase.

Increased disorder in the nanosheet structure determined by fitting of the D band region was the most distinctive feature of Raman spectra of GSG nanosheets. Increased D/G band ratio also suggested that distance between the defects in the nanostructures decreased [40]. There are two main groups of the defects in the graphene nanosheets structure: (a) zero-dimensional defects such as vacancies and dopant atoms described by the mutual distance L_D and (b) one dimensional defects represented by nanosheets edges and grain boundaries described by distance L_a [45]. Structure of GSG samples, nanosheets with tens and hundreds of nm in size, suggests a significant role of one dimensional defects in D peak intensity. As such, the D peak intensity and appearance of D' peak in Raman spectra was consistent with scattering from GSG nanosheets edges [46]. As far as the 2D band region was concerned, there were slight differences in the fitted peak intensity but its FWHM was constant at 54 cm^{-1}, suggesting the thickness of nanosheets was approximately the same. In general, the Raman spectra corresponded to disordered few-layer graphene. This observation was in agreement with the results of SEM where size and thickness of all GSG samples was very similar and therefore mainly influenced by the same amount of precursor delivered into the discharge. Detailed summary of the Raman spectroscopy analysis can be found in table 1.

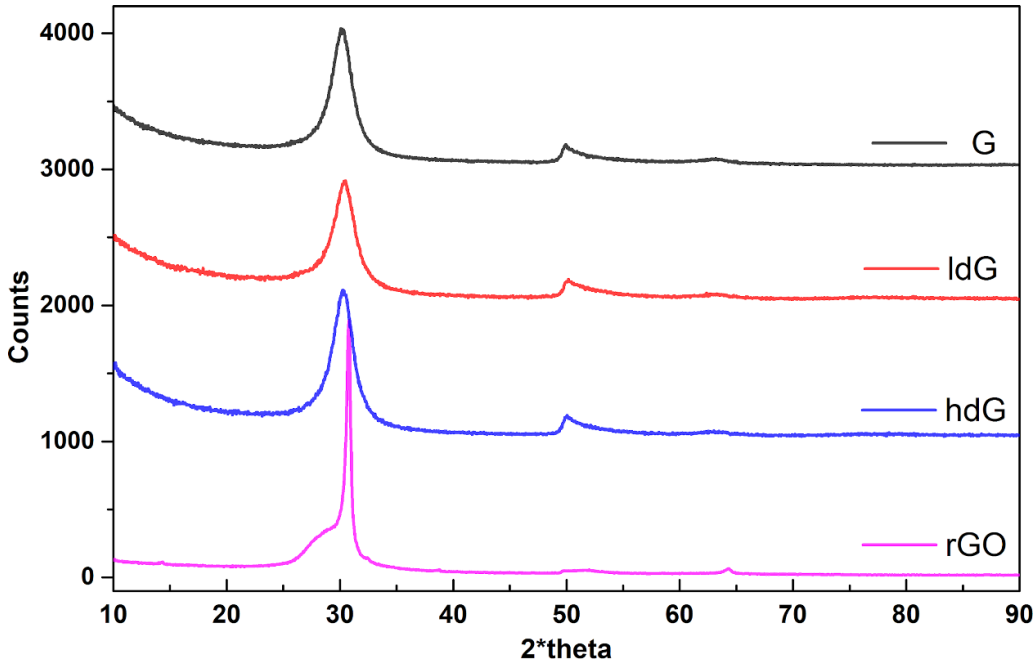

Figure 3. XRD characterization of prepared carbon nanomaterials ($\lambda_{K\alpha 1} = 0.178901$ nm).

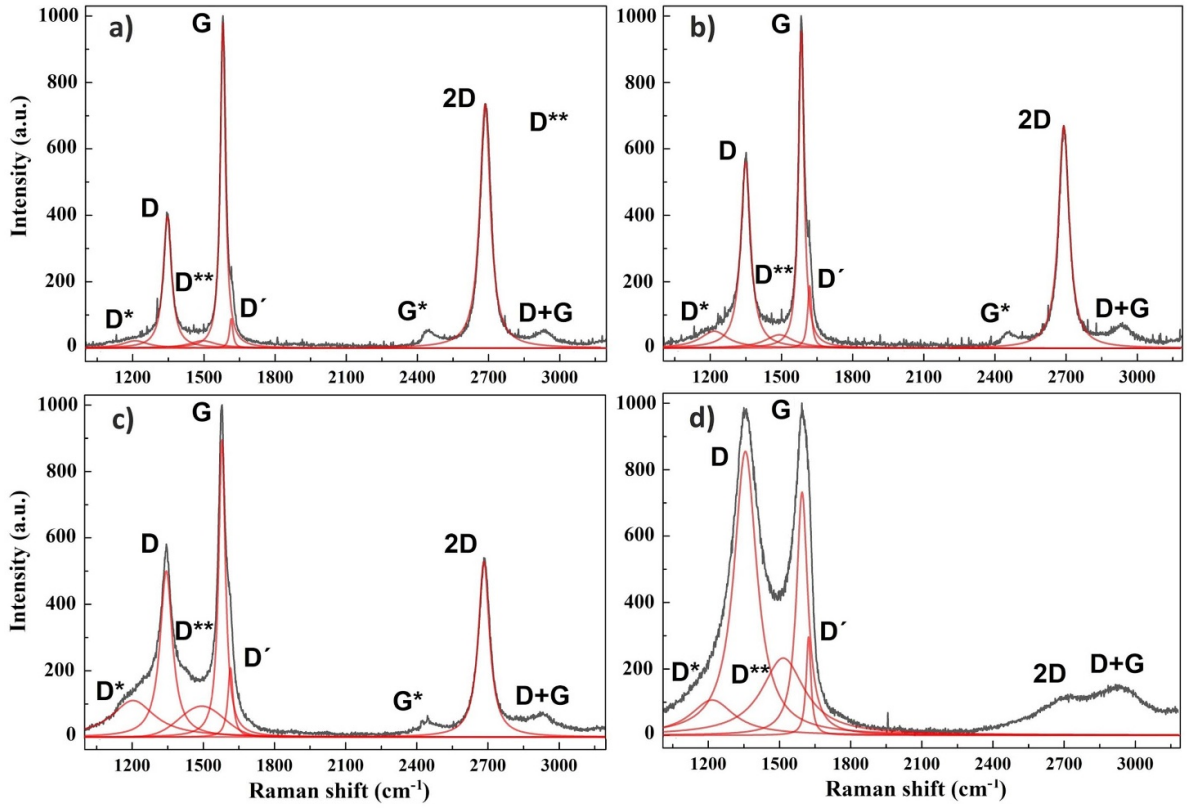

Figure 4. Raman spectra of GSG nanosheets and reduced graphene oxide samples, (a) G, (b) ldG, and (c) hdG and (d) rGO, respectively.

The rGO sample exhibited typical graphite oxide-like Raman signal (figure 4(d)), which was different from characteristic Raman spectra of GSG nanosheets. The difference in 2D band region was the most noticeable, since rGO structure was much thicker and thus its Raman spectrum corresponded to defective graphite structure with low 2D band intensity [40]. Raman spectrum was dominated by a broad high intensity D band region. Next to the main D peak, both defect activated shoulders at lower and higher wavenumbers (D^*—1210 cm^{-1} and D^{**}—1510 cm^{-1}) were observed. This

Table 1. Raman analysis of prepared carbon nanomaterials. G peak integrated intensity/area = 1. D/G = D peak intensity. 2D/G = 2D peak intensity.

Raman parameter/Sample	G	ldG	hdG	rGO
D^* Intensity	0.11	0.27	0.97	0.59
D position (cm^{-1})	1346	1348	1346	1348
D Intensity	0.64	1.05	1.53	2.48
D FWHM (cm^{-1})	42	50	60	116
D^{**} Intensity	0.11	0.20	0.51	1.28
G position (cm^{-1})	1580	1583	1578	1586
G FWHM (cm^{-1})	26	28	28	58
2D position (cm^{-1})	2688	2692	2689	
2D Intensity	1.54	1.35	1.32	
2D FWHM (cm^{-1})	54	54	56	
$(D^* + D' + D^{**})/G$	0.27	0.6	2.16	2.05

implied considerable structural imperfections and presence of large amount of defects in the reduced graphite oxide structure. The intensity of the D band remained high even after reduction and substantial decrease of amount of oxygen as determined by EDX and XPS analysis. According to the analysis method proposed by Sadezky [42], the high increase in the intensity of both, the D and D^* peaks, was caused by presence of the disordered graphitic lattice at the edges of the rGO flakes and defects in the plane of graphene layer. On the other hand, the analogous growth of the D^{**} band intensity was linked to the presence of a high fraction of amorphous carbon. Finally, the high intensity of the intra-valley defect (D') band in the rGO sample also confirmed the increase in the amount of defects and structural disorder.

3.4. XPS analysis

Samples were further characterized by XPS and the results showed that the GSG nanosheets contained from 96 at% to 98 at% of carbon and a small amount of oxygen. The rGO sample consisted of 92 at% of carbon and 8 at% of oxygen and a small amount of other impurities, such as sulfur and manganese This was in agreement with the results of EDX analysis. Detailed analysis of C1s peak of XPS spectra (figure 5) showed the presence of peaks centered at 283.5 ± 0.1 eV, 284.4 ± 0.1 eV and 285.2 ± 0.1 eV, which were assigned to sp, sp^2 and sp^3 hybridized carbon. Peak at lower binding energy, 283.5 eV, was assigned to sp hybridized carbon according to Rybachuk and Bell [47]. Further, there are theoretical density functional theory (DFT) calculations, which assign this peak to the presence of point defects in the hexagonal carbon lattice of the nanosheet structure [48, 49]. An alternative fit without using the sp peak could not properly reproduce the low energy part of the C1s spectra.

Carbon atoms bound to oxygen were also detected with peaks centered at 286.2 ± 0.2 eV, 286.9 ± 0.2 eV, and 288.1 ± 0.2 eV assigned to C–O, C=O carbonyl and O–C=O carboxyl groups, respectively. It was very important to properly deconvolute the C1s region to obtain results in conformity with the theory [50]. Several constraints were applied in C1s spectra deconvolution procedure. Background correction was performed applying Shirley algorithm. The peak of sp^2 component was modeled by using asymmetric Doniach–Šunjić (DS) profile [51] (asymmetry parameter 0.01) convoluted with Gaussian (100%)–Lorentzian (0%) pseudo-Voigt profile. For a metallic system such as graphite, graphene, or metallic CNTs (all sp^2 phase carbons), the C1s line will exhibit asymmetry towards higher binding energies due to the Kondo-like many-electron interactions of the metallic conduction electrons with the accompanying deep hole in the final state as described by Doniach–Šunjić. The asymmetry is zero for semiconductors and insulators, recovering the symmetric Lorentzian form of the line. Therefore, components describing sp^3 hybridized carbon or oxide groups bonded to carbon were modeled with symmetric Gaussian (70%)–Lorentzian (30%) pseudo-Voigt profile. The deconvolution of C1s peak profile can be seen in figures 5(d) and (a)–(c) for rGO and GSG samples, respectively. The highest sp^2/sp^3 ratio, 13.1, possessed graphene nanosheets G sample with 6.2% content of C–O, C=O, and COOH groups. The sp^2/sp^3 ratio decreased in ldG sample, 9.9, and was comparable to rGO sample with ratio of 11.3, but rGO sample contained 9.5% of carbon–oxygen groups (table 2).

3.5. Thermal stability of prepared nanomaterial

3.5.1. TGA. Detailed thermal stability study of synthesized carbon nanomaterials was carried out using TGA and DSC. In general, two properties can influence the oxidation temperature of carbon based nanomaterial: particle size and level of graphitization (disorder degree). According to experimental results of Morgan *et al* [52] and the shrinking core model, the particles with smaller diameter or size exhibit lower temperature of oxidation. On the other hand, structures with lower level of graphitization or with higher amount of defects are prone to combustion at lower temperatures, since defect sites are susceptible for any kind of disruption [28]. Generally, there are several regions found in TGA curves of carbon-based materials. The initial mass loss occurring at temperatures up to 100 °C corresponds to the release of water vapors from the carbon particle surface. Secondly, thermal decomposition of unstable oxygen-containing functional groups, especially hydroxyl and lactone groups [53], as well as intercalated water release, occurs at temperatures between 200 °C and 300 °C [54]. The graphene based nanomaterial itself begins to combust above 400 °C. The third temperature range between 400 °C and 500 °C reflects a decomposition of light amorphous polycarbons to carbon dioxide that are easily vaporized [55]. The last region indicates gradual destruction of the most stable phase of graphene structure above 700 °C due to the breaking of C–C bond and complete oxidation of carbon in synthetic air [56].

Brief information about thermal stability of GSG nanomaterial was reported by several authors. Melero *et al* [57] used (Torche à Injection Axiale sur Guide D'Onde) TIAGO torch for the synthesis of CNTs and graphene nanosheets without use of catalyst and investigated their thermal stability in air and the results of the analysis showed single oxidation temperature at 554 °C further proving a very clean deposit with no amorphous phase and low amount of defects.

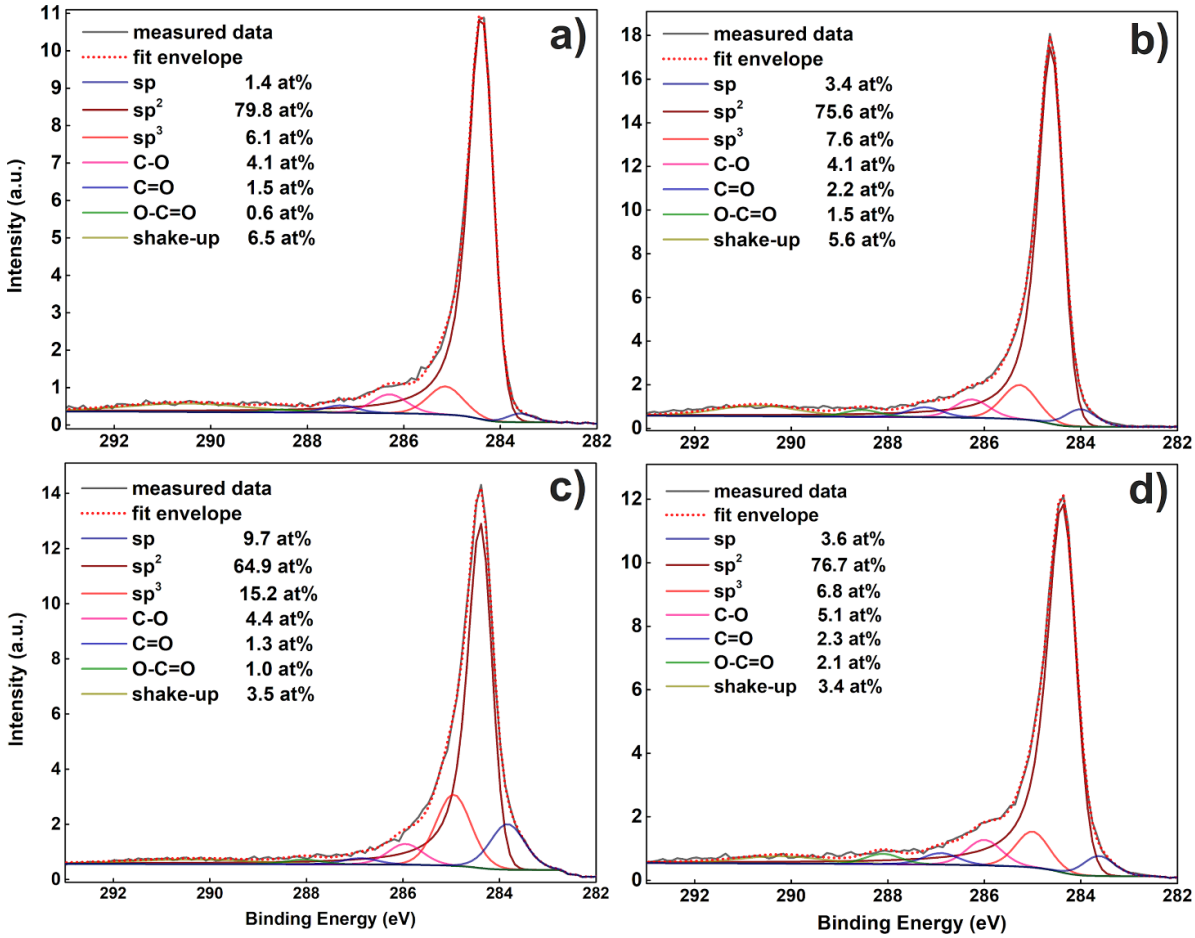

Figure 5. XPS C1s spectra of GSG nanosheets and reduced graphene oxide samples, (a) G, (b) ldG, and (c) hdG and (d) rGO, respectively.

Table 2. XPS analysis of prepared carbon nanomaterials. C cont. = overall content of carbon in the sample.

Sample/C1s peak analysis	sp	sp^2	sp^3	C–O	C=O	O–C=O	π–π^*	C cont. at%	O cont at%.	C/O ratio
G	1.4	79.8	6.1	4.1	1.5	0.6	6.5	98.3	1.7	57.8
ldG	3.4	75.6	7.6	4.1	2.2	1.5	5.6	97.6	2.4	40.7
hdG	9.7	64.9	15.2	4.4	1.3	1.0	3.5	95.9	4.1	23.4
rGO	3.6	76.7	6.8	5.1	2.3	2.1	3.4	92.3	7.7	12.0

Fronczak *et al* [58] investigated growth of various graphene nanostructures including nanosheets in radiofrequency plasma jet using a wide range of alcohols and investigated stability of these structures by TGA/DSC analysis. They showed that similarly to results of Dato and Frenklach [36], except ethanol, other alcohols possessing O/C ratio from 0.1 to 0.5 produce mostly amorphous structures but with higher carbon yield. Thermal stability of these structures investigated by TGA analysis increased with increasing O/C precursor ratio or addition of oxygen to decanol precursor. The DTG curve of the nanostructures was divided into three groups according to temperatures: (a) 550 °C–600 °C, (b) 640 °C–690 °C, and (c) 700 °C–750 °C. Amount of the first group was above 40% for all studied precursors and only ethanol, propanol, and butanol had a significant amount of third group. Except for decomposition of ethanol in MW plasma, high temperature plasma discharges such as arc discharge and plasma torches were used for graphene nanoflakes synthesis. AC arc discharge with carbon electrodes in the N_2/H_2 atmosphere was used for carbon nanopowder synthesis by Wu *et al* [59]. The produced nanosheets were five layers thick and their quality varied with change of N_2/H_2 ratio. This method could produce 2.1 g of nanopowder in 5 min and its stability was investigated by TGA analysis with a single peak at 673 °C showing high purity of graphene. Amirov *et al* [60] used DC plasma torch in Ar/He with methane to produce porous multi-layer graphene which started to decompose in air at 300 °C and main weight loss occurred around 550 °C. The synthesis methods of various carbon nanomaterials and their TGA/DTG results are summarized in table 3.

TGA of nanomaterials prepared by two distinct processes showed clear difference between structural and chemical

Table 3. Summary of plasma synthesis of graphene nanosheets, their TGA analysis and comparison with other carbon materials. AC—alternating current, DC—direct current, RF ICP—radiofrequency inductively coupled plasma, CVD—chemical vapor deposition.

Method of synthesis	Discharge atmosphere	Precursor	TGA atm.	Heating rate (°C min^{-1})	DTG peak (°C)	Ref.
AC arc discharge	N_2/H_2	Solid carbon	Air	10	650	[59]
TIAGO MW torch	Ar	Ethanol	Air	5	554	[57]
RF ICP torch	Ar	Ethanol	N_2/O_2 95/5	10	704	[58]
DC plasma torch	Ar/He	Propane-butane	Air	10	630	[60]
Electrochemical	Electrolyte	Graphite	Air	NA	500–700	[61]
Alkali metal intercalation based exfoliation	Ar/vacuum	Graphite	N_2	NA	500–1000	[62]
Joule heating	Air	Anthracite coal	Air	NA	700	[5]
Ultrasonication	Ethanol liquid	Graphite	N_2	NA	300–600	[63]
MW plasma torch	Ar	Ethanol	Air	10	750	This work
CVD CNT	Ar/H_2	Ethylene	Air	5	665	[64]
C_{60} powder	Commercial	Solid carbon	O_2	20	600	[29]
Diamond powder	Commercial	Natural	O_2	20	710	[29]
Graphite powder	Commercial	Natural	O_2	20	850	[29]

composition of carbon nanosheets and nanoplatelets. After the first derivative of the TGA curves (DTG curve), we could observe several temperature (thermal stability) ranges with specific temperature positions of peak maxima for each of the studied carbon nanostructures. The positions, halfwidth and areas of the peaks were obtained by the deconvolution procedure using Fraser–Suzuki asymmetric profile [65]. GSG nanosheets and rGO samples exhibited different number of thermal stability ranges and their fractions.

Figure 6 shows TGA measurements of all four types of samples discussed in our study. It can be seen that the thermal stability of each of them was different and could be deconvoluted with different number of Fraser–Suzuki profiles. The results obtained from Raman spectroscopy, XPS and electron microscopy enabled us to establish a connection between the composition of each of the studied materials and their thermal stability (i.e. shape of the DTG curve).

The chemical reduction and heat treatment of rGO sample led to the release of water and removal of labile oxygen functional groups found between 50 °C and 300 °C. Most disorder carbon phase with predominantly carboxyl, hydroxyl and lactone groups, and light polycarbons was removed as well. DTG curve of rGO sample could be deconvoluted into two components, at 545 °C and 607 °C, related to the oxidation process, formation of CO and CO_2, of the main structure of nanoplatelets. This simplified the DTG curve shape greatly in comparison to partially rGO materials [66].

Figures 6(a)–(c) show TGA/DTG curves of GSG samples synthesized in MPT. It can be seen that the samples behaved differently, which can be attributed to the controlled process of their synthesis. Thus, DTG curves of well graphitized graphene nanosheets exhibited single major peak with temperature of full oxidation, up to 810 °C. DTG curve profile gradually changed from three peaks, at 345 °C, 570 °C and 763 °C, for defective structures of hdG sample to single narrow peak at 751 °C with very small addition of peak at 571 °C for graphene nanosheets G sample. Shape of the DTG curve of GSG samples could be understood from Raman and XPS analysis of the samples. Overall, the samples contained only a small amount of oxygen, 1.7 at%, 2.4 at% and 4.1 at% for G, ldG, and hdG samples, respectively. C1s XPS peak analysis showed between 6% and 8% content of carbon–oxygen groups in the samples. Low oxygen content explained the missing part of the DTG curve related to decomposition of structure with oxygen related groups around 200 °C. However, as can be seen from Raman spectra (figure 4), the difference between the GSG samples was the amount of disorder in their structure. The amount of disorder, D*, D, D** and D′ Raman peak intensity, increased in samples synthesized in turbulent gas flow or low delivered MW power conditions. This fact was supported by decrease of sp^2/sp^3 ratio in XPS spectra from 13.1 to 4.3 for G and hdG sample, respectively. This correlated with the fact that most thermally stable nanosheets showed highest sp^2 carbon phase content together with the lowest D band intensity according to Raman spectroscopy. As a consequence, DTG curve of ldG and hdG samples exhibited low intensity peak 345 °C related to amorphous phase in the nanosheet structure which was missing in the G sample. All samples exhibited peak at 570 °C. The area of this peak decreased with increasing sp^2/sp^3 ratio and decreasing D/G ratio in the prepared samples. Therefore, sample G exhibited only a very low intensity effect at 570 °C at DTG curve, which can be described with a fit of just a single peak.

In general, the position of this final oxidation process peak varied between samples from 724 °C to 763 °C. Except for the amount of disorder and particle size, an important property for oxidation process rate was surface area of the material [67]. As a rule of thumb, higher the surface area, the faster decomposition of the sample was expected. In our case, we investigated this dependence for G type samples. Two samples prepared under the same deposition conditions exhibiting the same DTG curve profile, but different third peak position, were used for surface area analysis by BET method. The results showed that the sample with lower temperature of final oxidation peak, 751 °C vs 771 °C, had a surface area of 881 m^2 g^{-1} in comparison to 348 m^2 g^{-1} of the second sample. The surface area of the sample was several times larger than the values reported for GO nanopowder [68] which further proved high

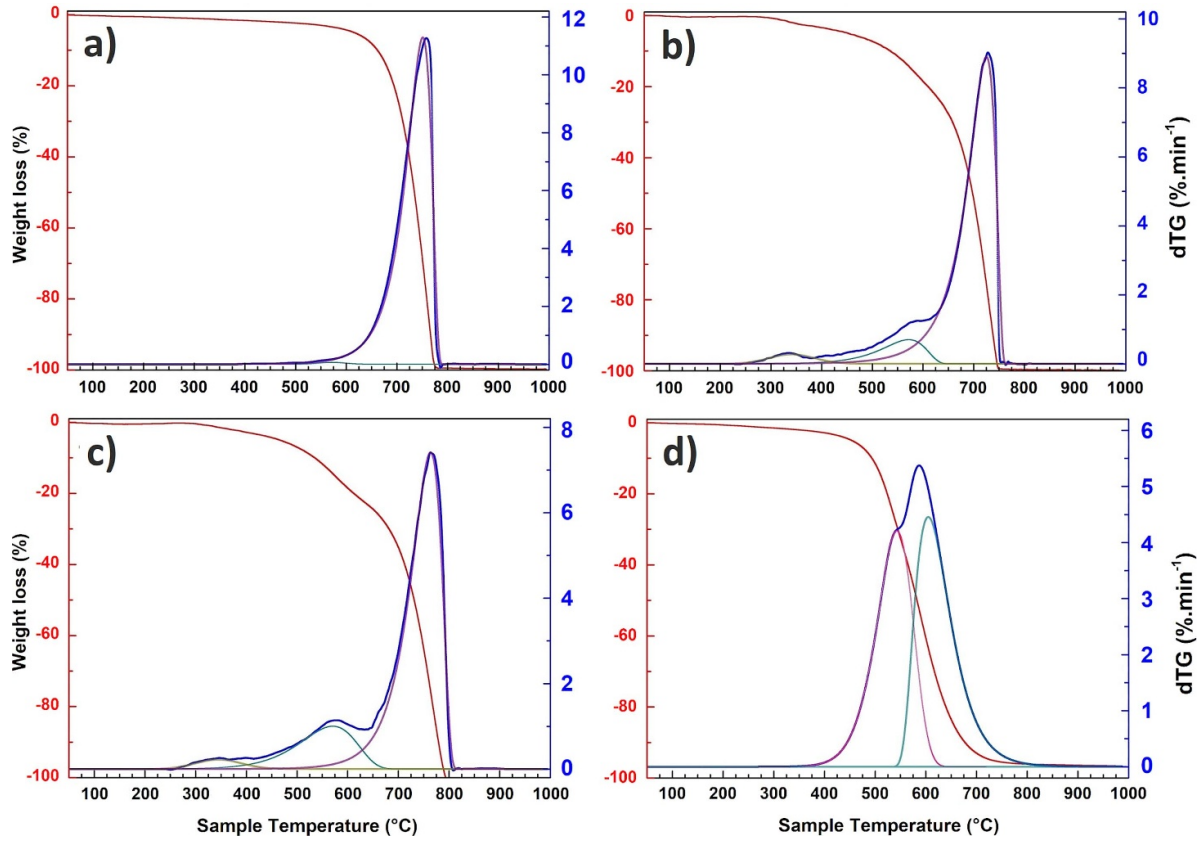

Figure 6. TGA(red)/DTG(dark blue) analysis of prepared carbon nanomaterials: (a) G, (b) ldG, (c) hdG and (d) rGO.

oxidation resistance of GSG material. In general, the thermal stability of rGO (figure 6(d)) was lower than GSG samples and was mainly influenced by high amount of disorder, as determined from Raman D peak intensity, even with relatively low oxygen content of 7.7 at%.

We also investigated the influence of heating rate on the oxidation process during the sample analysis. In literature, various heating rates were used for analysis of graphene based materials, from 1 °C min^{-1} to 25 °C min^{-1}. Lowest heating rates are usually used to avoid the violent process of thermal expansion of GO during the analysis. It is also expected that with the lower heating rate the TGA curve effects will shift to lower temperature and its FWHM would be smaller due to the exposure of the sample to given temperature for longer time. In our case, we used an intermediate rate of 10 °C min^{-1} which was used by Fronczak *et al* [58] in their study and we did not experience any problems with instability of our samples. To study the influence of the heating rate on the position of the TGA curve, we carried out an analysis of the G sample at a heating rate of 2 °C min^{-1}. This way we could compare our result with the only other TGA analysis of graphene nanosheets synthesized in MW plasma reported by Melero *et al* [57] which used a heating rate of 5 °C min^{-1} and reported a single peak at 554 °C. As expected, our DTG curve shifted to lower temperatures (figure 7), but we observed only moderate shift of the oxidation peak position from 751 °C to 681 °C, further proving high thermal stability of our graphene nanosheets.

Besides analysis of DTG curve, each sample heat flow measurement was analyzed as well (figure 8). The only source of heat in our measurement was the oxidation reaction of carbon and oxygen. In our main reaction interval, between 300 °C and 800 °C, the formation of CO_2 was favored over CO with main exothermic reaction

$$C + O_2 \rightarrow CO_2, \quad (1)$$

yielding 394 kJ of energy per mol [69]. We analyzed the heat flow curve's profile for each sample and found it to be in agreement with DTG curve's profile. This observation can be explained by the direct relationship between content of each material fraction and its thermal stability. Oxidation process (1) of each fraction then yields proportional amounts of energy in the form of heat. At temperatures around 300 °C and 570 °C, the heat release can be attributed to CO_2 formation by reaction of oxygen with released carbon–oxygen functional groups and disorder phase of GSG nanosheets structure. Above 600 °C, the most stable fraction of material underwent oxidation reaction, while releasing the heat with temperature profile and magnitude matching that observed on DTG curve. This way, the heat release from the material can be varied based on fraction content and controlled by the synthesis conditions of GSG nanosheets. As mentioned in the Introduction section, such property is of practical importance in the application of such material as an advanced flame retardant. Lower oxidation resistance of rGO led to the maximum heat release at 590 °C.

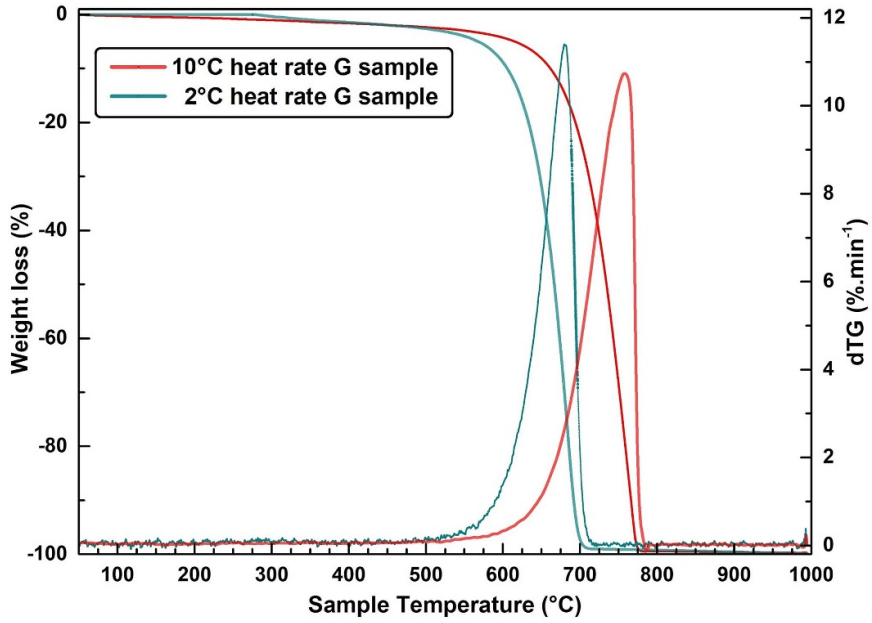

Figure 7. Comparison of TGA/DTG curves of G sample with different heating rates.

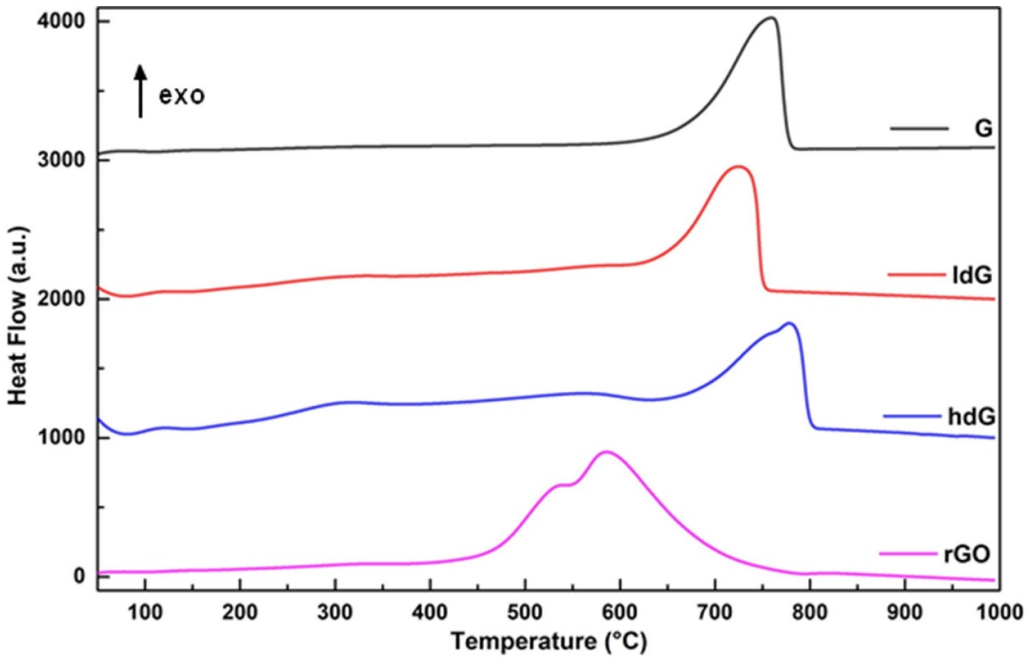

Figure 8. DSC heat flow curves of prepared carbon nanomaterials (10 °C min^{-1}, 20 sccm air).

3.5.2. Investigation of high oxidation resistance of GSG nanosheets by thermal annealing. TGA led to observation of clear differences between thermal stability of various GSG nanosheets samples, but the underlying changes in the samples could not be analyzed during the analysis. Therefore, we carried thermal annealing of GSG samples at relevant temperatures chosen on the basis of TGA results. In such a way we could determine underlying structural and chemical changes in the disordered GSG nanosheets structure at high temperatures. The samples were annealed in the synthetic air atmosphere at temperature range from 350 °C to 750 °C and analyzed by Raman spectroscopy and XPS (table 4).

The G sample structure, as expected, did not exhibit any changes until the temperature reached 600 °C, where it began to be affected by the oxidation process. The oxidation process started at the defects in the graphene nanosheets structure and slowly began to affect the whole structure. Above 700 °C, the GSG nanosheets underwent full oxidation starting from defective sites and edges, until full disintegration of the nanosheet structure was reached. The same process, but

Table 4. Raman and XPS analysis of hdG samples at 345 °C and 570 °C, respectively. C cont. = overall content of carbon in the sample. G peak integrated intensity/area = 1. D/G = D peak intensity. 2D/G = 2D peak intensity.

Raman analysis parameters	hdG-345	hdG-570	XPS C1s peak analysis	hdG-345	hdG-570
D^* Intensity	0.61	0.19	sp	2.7	2.3
D position (cm^{-1})	1344	1345	sp^2	78.4	86.2
D Intensity	0.97	0.78	sp^3	7.3	1.4
D FWHM (cm^{-1})	52	40	C–O	3.6	3.0
D^{**} Intensity	0.45	0.19	C=O	1.7	1.4
G position (cm^{-1})	1576	1578	O–C=O	0.8	0.7
G FWHM (cm^{-1})	32	26	π–π^*	5.5	5.0
2D position (cm^{-1})	2686	2685	C cont. at%	97.5	98.5
2D Intensity	1.01	1.59	O cont. at%	2.5	1.5
2D FWHM (cm^{-1})	62	56	C/O ratio	39	65.7
$(D^* + D' + D^{**})/G$	1.25	0.48			

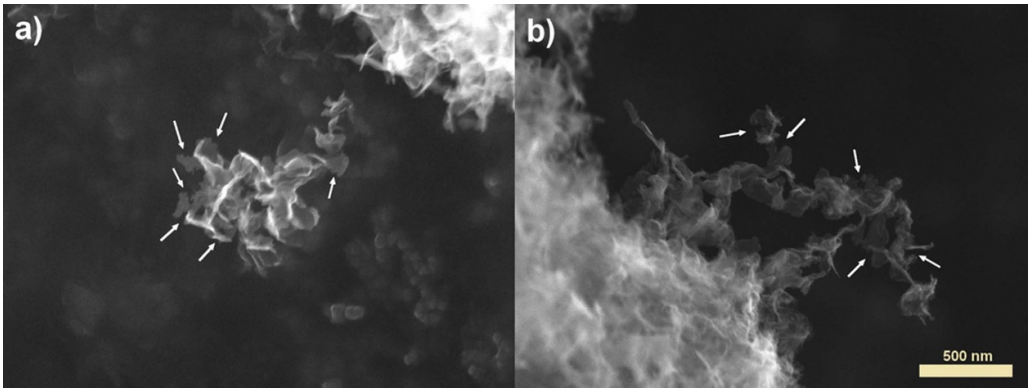

Figure 9. SEM analysis of annealed samples at 700 °C: (a) G sample in humid air (b) hdG sample in synthetic air, arrows indicate defects in the structure of nanosheets.

at slightly lower temperature, was observed in case of hdG sample and G sample annealed at the presence of humidity in the ambient air atmosphere (figure 9), where the disintegration process was faster with partial stability of the nanosheets up to 600 °C and almost complete burnout of the sample at 700 °C. In both types of sample, we could observe deformation of nanosheet shape and partially removed sections of its structure. This led to formation of large amount of defects and fast removal of nanosheets by oxidation reaction.

This process was clearly reflected in the D and G band intensities of annealed samples. Raman spectra of the G sample annealed at 345 °C and 570 °C showed no significant differences and only at the higher temperatures could we observe an increase of D/G Raman band ratio from 0.6 to 0.9 (figure 10). At the same time, 2D/G peak ratio remained the same (figure S2).

On the other hand, there were substantial differences in the stability of graphene nanosheets with a larger amount of disordered phase, hdG sample (figure S3). The annealing at 345 °C did not lead to significant decrease of D^* and D^{**} band intensity (figure 11(a)) and therefore the intensity of these peaks can not be conclusively used as a measure of a highly disordered phase in our samples. However, annealing at 570 °C (figure 11(b)) led to almost complete elimination of D^* and D^{**} band in its Raman spectra.

Besides for structural disorder, the amount of oxygen can have a significant impact on thermal stability of carbon nanostructures. Therefore, graphene-based nanomaterials with low oxygen content exhibit higher oxidation resistance. Plasma-based synthesis of GSG results in very low oxygen content with carbon to oxygen ratio of 50:1 or less. Except GSG, Achee *et al* [61] reported high yield electrochemical exfoliation of graphite with low oxygen content and thermal stability between GO and parent natural graphite flakes. Recently, Luong *et al* [5] reported graphene nanosheets and carbon polyhedra synthesis, called flashed graphene (FG), by rapid Joule heating of inexpensive carbon sources—such as anthracite coal and coffee grounds, petroleum coke, carbon black, etc, with purity of up to 99%. TGA in air of anthracite coal FG showed maximum mass loss at around 700 °C. MW-assisted solvothermal method was used by Van Khai *et al* [70] for production of highly conductive few-layer graphene with low oxygen content (6.5 at%) and morphology similar to GO. Munuera *et al* [71] used top-down anodic exfoliation with highly oriented pyrolytic graphite as well as graphite foil, flakes and powder as electrode and showed that proper choice of initial material, graphite foil, allowed them to produce biocompatible graphene with low or high oxidation ratio O/C of 0.058 and 0.110, respectively. Alkali metal intercalation method was used by Park *et al* [62] for exfoliation of

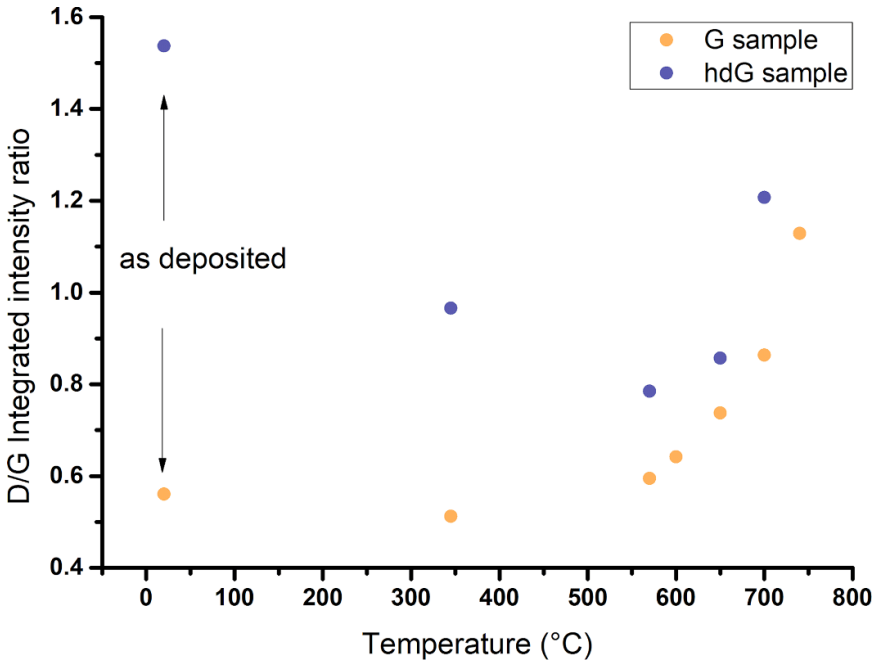

Figure 10. Dependence of D/G peak ratio on sample annealing temperature.

graphite flakes in inorganic solvents, forming stable dispersion without any functionalization and surfactant. Produced flakes had 2–3 at% of oxygen and experienced main mass loss under N_2 atmosphere above 500 °C. Greco *et al* [63] used liquid phase exfoliation of graphite flakes in *N*-methyl-2-pyrrolidone and ethanol under ultrasound and produced Si nanoparticles/few-layer graphene composite for Li-ion battery anodes. These structures had low D/G ratio around 0.5 and TGA under N_2 atmosphere showed the main mass loss in the range from 300 °C to 600 °C. Shear exfoliation in liquids and ball milling in solvents were used for production of graphene flakes with various oxygen contents as well. These methods were recently reviewed by Kairi *et al* [2].

XPS analysis of annealed hdG sample (figures 11(c) and (d)) showed sp^3 phase content decreased from 15.2 to 7.3 and 1.4 at% for 345 °C and 570 °C annealing temperature, respectively. The annealing led to moderate decrease of carbon–oxygen functional groups, mainly lowering the C–O and C=O groups content. The decrease of content of C–O and C=O groups with increasing temperature was in agreement with results of molecular dynamics simulations [72] and experimental observation of decomposition of various types of oxygen functional groups by Figueiredo and Pereira [73]. Overall oxygen content decreased to 1.5 at% further confirming chemical composition similarity between hdG-570 and G type nanosheets (table 4). Regarding sp carbon hybridization content, only a small decrease of sp content was observed, which left only sp^3 phase content as a good measure of disordered carbon structure.

Therefore, the results of Raman and XPS spectroscopy led to the conclusion that after annealing at 570 °C, only high quality graphene nanosheets are left in the sample. This is in agreement with TG analysis of hdG sample, where the last part of the DTG curve reached the same temperature as G sample. The synthesis conditions of hdG sample led to formation of large fraction disordered phase and small nanosheets, below 10 nm, with free dangling bonds on its edges, as observed in TEM images (figure 2(c)). These fractions were removed after annealing at 345 °C and 570 °C and correspond to the peaks observed in the DTG curve. Last part of the DTG curve was formed by large sheets, with curved edges and low amount of defects in their structure. Further increase of the annealing temperature to 700 °C led to the disruption of nanosheets edges and its shape as can be observed in figure 9.

We determined activation energy of defect formation under oxidation atmosphere by applying the following relation between D/G band intensity ratio and process activation energy E_a,

$$I_D/I_G = A_1 e^{-Ea1/kT} + A_2 e^{-Ea2/kT}, \quad (2)$$

as suggested by Liu and Zhang [74], where k is the Boltzmann constant and T is process temperature. In our case, activation energy (E_{a1} and E_{a2}) denotes energy required to initiate defect formation in the nanosheets structure caused by reaction of carbon and oxygen atoms. Please note that activation of these defects was not observed in an inert atmosphere. For the hdG sample, the curve had non-trivial shape (figure 10), because the intensity of D peak at first decreased with removal of disorder fraction of the material and increased only after annealing above 650 °C.

The G type sample dependence could be fitted with a combination of two exponential functions with E_{a1} of 2.0 eV and E_{a2} of 0.6 eV, corresponding to two kinds of defect generation processes (figure 12). These two processes are responsible

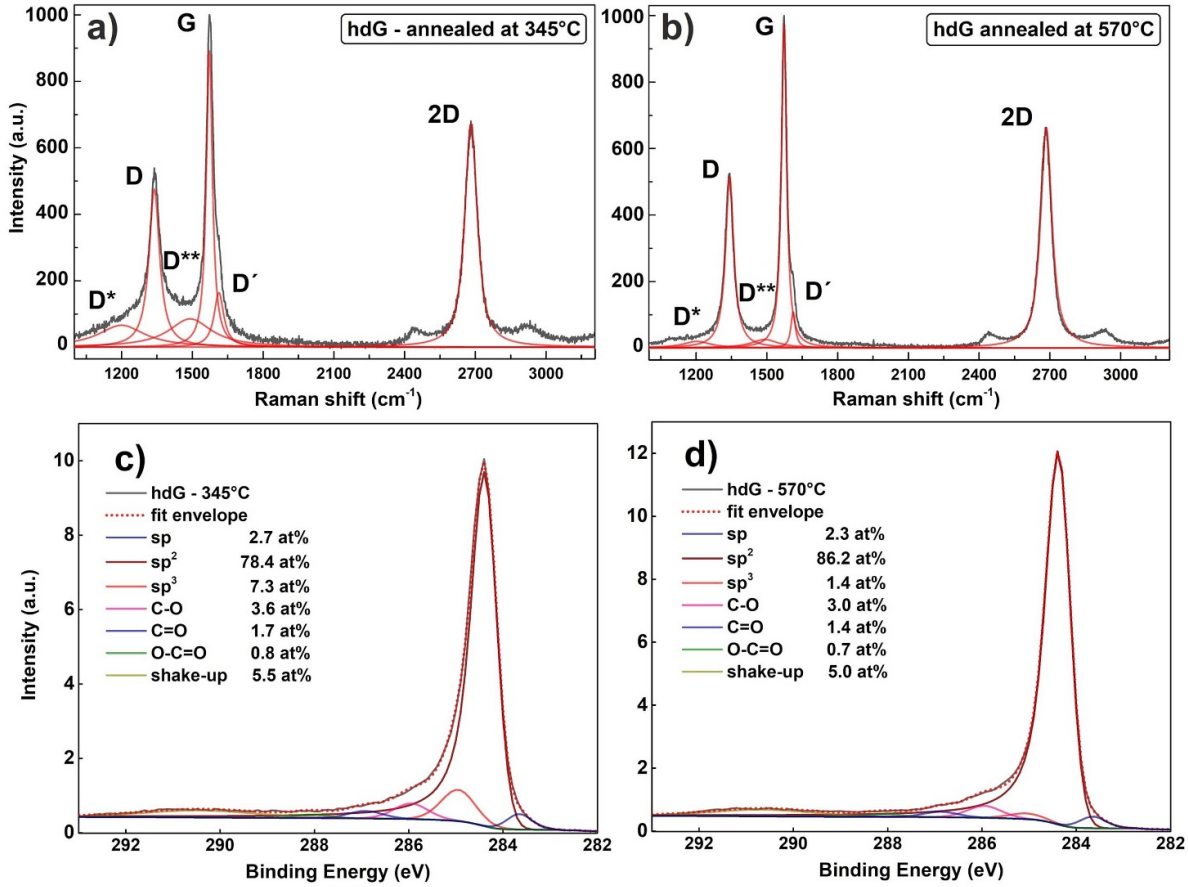

Figure 11. Raman and XPS analysis of graphene nanosheets annealed at 345 °C: (a) Raman spectra, (c) XPS C1s spectra; and 570 °C: (b) Raman spectra, (d) XPS C1s spectra, respectively.

for DTG curve peaks at 570 °C and 700 °C. This is in agreement with our DTG analysis of G sample (figure 6(a)), where a nonzero contribution of peak at 570 °C was observed.

The E_{a1} value of activation energy of carbon oxidation of main nanosheets structure was higher than the value found for graphite oxidation, 1.6 eV [67], but in agreement with value reported for defects formation by oxidation process of bi-layer graphene on the substrate [74]. Such a large energy barrier is also enhanced by the mutual twist of graphene layers in our multilayer structure as described in sample TEM analysis. It was shown by molecular dynamics simulation [75] that twisted graphene layers with size of several tens of nanometers remain stable up to several thousand Kelvin with activation energy barrier of untwisting of more than 4 eV. Another mechanism leading to stabilization of graphene sheets can be hydrogen bonded to free carbon dangling bonds as shown by Zhong and Hong [27]. We cannot exclude this stabilization process as well, however according to Dato *et al* [76], few layer graphene nanosheets prepared by MW plasma decomposition of ethanol contain only 1 at% or less of hydrogen and most of the hydrogen from the precursor is converted to C_2H_2 and H_2 gas which escapes the experimental setup.

3.5.3. Fingerprint behavior of GSG nanosheets during high laser power Raman spectroscopy. High temperature stability of GSG nanosheets enabled us to carry out investigation using high power laser Raman spectroscopy. Except for changes in chemical composition and structural features, the GSG nanosheets also exhibited systematic deviation in behavior when irradiated with a high power laser beam. This became evident in development of D/G and 2D/G ratio during the measurements. G sample exhibited a significant decrease of 2D/G ratio with increasing laser power (figure 13) and similar, but weaker dependence was observed for its D/G band ratio. In hdG type sample, both ratios depended only very weakly on the laser power, but its behavior changed after annealing at 570 °C, when the sample response was consistent with G sample. The response of rGO sample was similar to the unannealed hdG sample and showed almost no dependence on the laser power. Contrary to us, Ferreira *et al* [77] observed a decrease in D/G band ratio with increasing power, $\lambda_L = 532$ nm, in the range from 0.5 to 3 mW in samples of multilayer graphene oxide (MLGO) and reduced MLGO. These materials also exhibited the shift of G band position and increase of its FWHM with increasing laser power, while mechanically exfoliated multilayer graphene showed no such

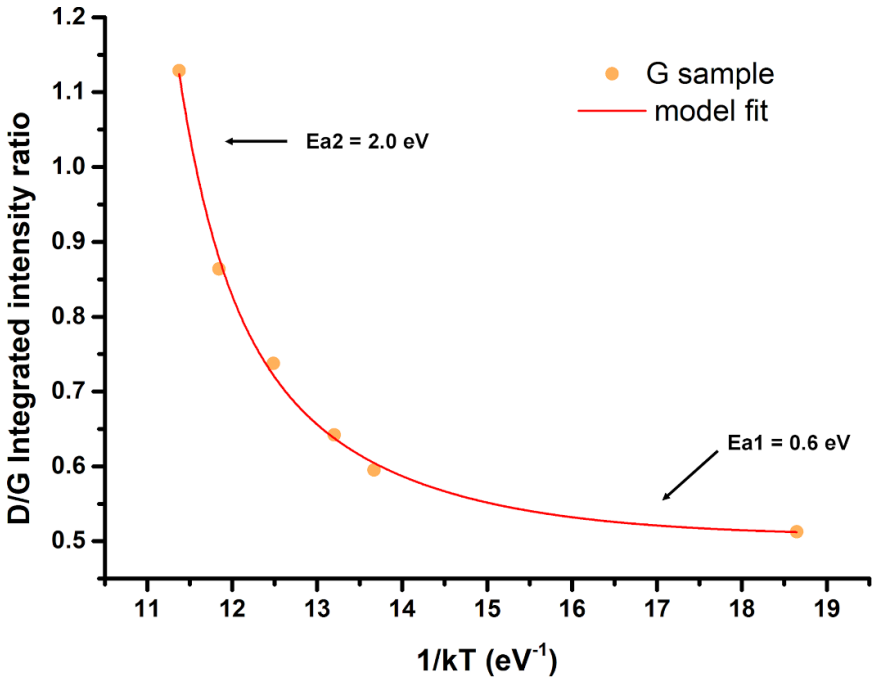

Figure 12. Activation energy model fit for G type annealed sample.

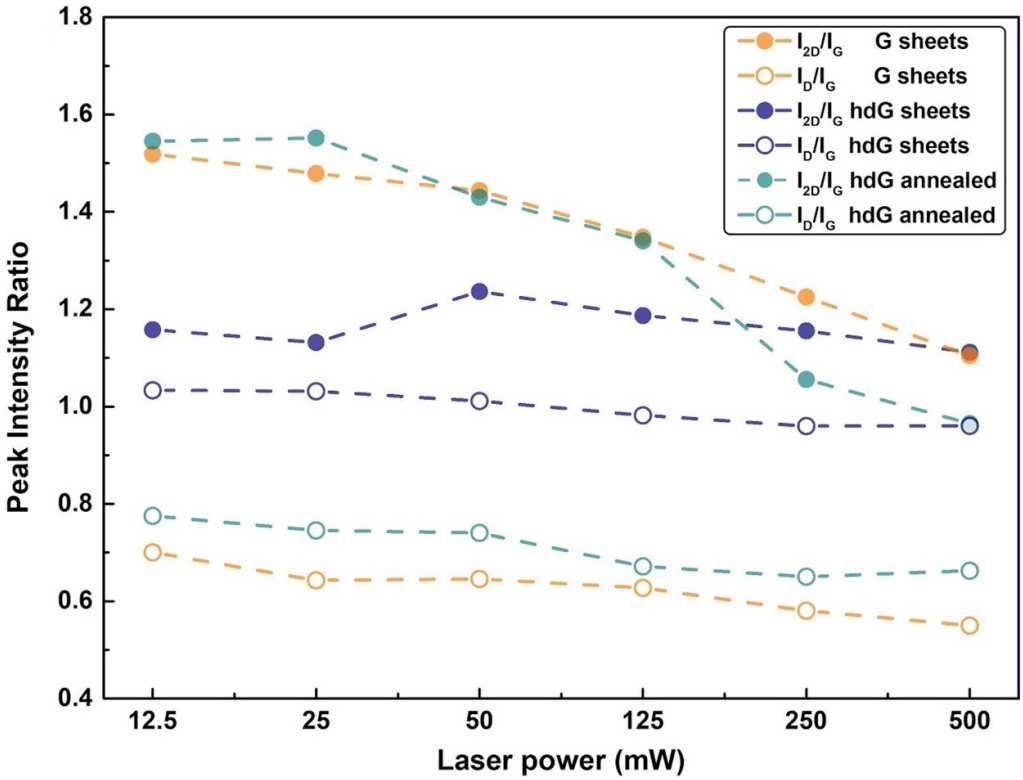

Figure 13. Comparison of laser power dependence of normalized Raman peak intensities for G (orange), hdG (blue) and hdG-570 (cyan) samples. Spot size diameter 2 μm, $E_{\mathrm{L}} = 2.34$ eV ($\lambda = 532$ nm).

dependence. The shift of Raman band positions is a known effect due to thermal expansion of crystal structure and anharmonic coupling of the phonon modes [78], and is linearly dependent on crystal temperature. The temperature coefficient is approximately between -0.01 and -0.03 cm^{-1} K^{-1} for sp^2 related carbon nanostructures but the measured value strongly depends on conditions of the measurement and nature of the sample. Similar behavior was also observed in our samples as the material started to be heated with increasing laser power. As mentioned above, the relationship between D and 2D band

intensity in graphene is non-trivial and the same is valid for behavior of response of our samples. In transition from single-layer graphene to disordered few-layer graphene, one would expect the increase of D/G ratio and almost complete elimination of the 2D band. This is not our case and the decrease of 2D band intensity is most probably related to increase of electronic linewidth as discussed by Venezuela *et al* [79]. Electronic linewidth is dependent on several parameters such as defects density, electron-phonon and electron-electron (doped sample charging) scattering and its increase leads to suppression of double resonance conditions.

In our hdG sample, the disordered structure most probably blocked any significant change of scattering parameters and its structure interacting with laser beam was saturated with defects which resulted in no change of D/G and 2D/G band ratio.

One should note that in our case high laser power, 500 mW at maximum, was needed to observe the effect in our sample. At the same time, even repeated measurements at the same spot exhibited only very small deviations, below 5%, and thus further confirmed high stability of our nanosheets. This measurement could also be carried out at constant power and variation of laser light flux could be achieved by applying different objective lenses (10×, 50×, 100× magnification) and the same dependencies were observed. This 'fingerprint' behavior can be easily used to distinguish nanosheets with various properties without the need of more difficult and time-consuming analysis such as electron microscopy or XPS, where these systems are difficult to distinguish before reaching a high degree of disorder. The sample response showed high correlation with results of TG/DSC analysis and could be used for the estimation of thermal stability of given material.

4. Conclusions

In conclusion, the gas phase synthesized graphene nanosheets prepared in MW plasma exhibited superior thermal stability, up to 750 °C, in comparison to graphene nanoplatelets prepared by liquid exfoliation and thermal expansion technique. Structural and chemical composition changes at high temperatures were investigated by thermogravimetry and thermal annealing. Few-layer graphene nanostructures with low oxygen content, less than 10 at% of carbon–oxygen groups, exhibited three thermal stability regions. These regions were found around 345 °C, 570 °C and above 700 °C and corresponded to three types of structure: amorphous and carbon–oxygen functional groups, small defective nanosheets overlaying main structure and highly crystalline structure with curved edges, respectively. Fraction size belonging to the corresponding structure can be directly estimated from the evaluation of DTG curve and controlled by synthesis conditions. The maximum temperature reached during TGA analysis was inversely proportional to material active surface area determined by BET technique. The high thermal stability and oxidation resistance of GSG nanosheets was supported by high activation energy of the oxidation process of 2 eV. MW plasma synthesized nanosheets exhibited reproducible distinctive response to high power laser irradiation during Raman spectroscopy which could be used to predict nanosheet thermal stability. This 'fingerprint' behavior, decrease of D/G and 2D/G band intensity ratio, could serve as a simple tool to differentiate between various graphene nanostructures and estimate their oxidation resistance.

The possibility to directly control high temperature oxidation resistance during the gas phase synthesis opens new opportunities for large scale applications in the fields of battery electrodes, fire retardants, sensors and advanced composite materials. Furthermore, the precise information about the relationship between the temperature stability of gas phase synthesized graphene and its chemical and structural changes provides valuable insight into the role of temperature fluctuations caused by MW plasma instability during its synthesis process.

Acknowledgments

This work was supported by The Czech Science Foundation under project 18-08520S and in part by project LM2018097 funded by the Ministry of Education, Youth and Sports of the Czech Republic. This work was also partially supported by the State Task of Ministry of Science and Higher Education of Russia (code FSUN-2020-0008). We would like to thank Jiri Bursik for TEM analysis.

Conflict of interest

The authors declare no conflicts of interests.

ORCID iDs

Ondřej Jašek https://orcid.org/0000-0002-1416-794X
Miroslav Šnírer https://orcid.org/0000-0003-0534-5262
Dušan Hemzal https://orcid.org/0000-0002-5822-9372
Alexander G Bannov https://orcid.org/0000-0001-5868-9013

References

[1] Novoselov K S, Jiang D, Schedin F, Booth T J, Khotkevich V V, Morozov S V and Geim A K 2005 Two-dimensional atomic crystals *Proc. Natl Acad. Sci.* **102** 10451–3
[2] Kairi M I, Dayou S, Kairi N I, Bakar S A, Vigolo B and Mohamed A R 2018 Toward high production of graphene flakes—a review on recent developments in their synthesis methods and scalability *J. Mater. Chem.* A **6** 15010–26
[3] Kazemizadeh F and Malekfar R 2018 One step synthesis of porous graphene by laser ablation: a new and facile approach *Physica* B **530** 236–41
[4] Dato A 2019 Graphene synthesized in atmospheric plasmas—a review *J. Mater. Res.* **34** 214–30
[5] Luong D X *et al* 2020 Gram-scale bottom-up flash graphene synthesis *Nature* **577** 647–51
[6] Mohan V B, Lau K-T, Hui D and Bhattacharyya D 2018 Graphene-based materials and their composites: a review on

production, applications and product limitations *Composites* B **142** 200–20
[7] Zhu Y X, Duan C Y, Liu H Y, Chen Y F and Wang Y 2017 Graphene coating for anti-corrosion and the investigation of failure mechanism *J. Phys. D: Appl. Phys.* **50** 114001
[8] Bannov A G, Prášek J, Jašek O and Zajíčková L 2017 Investigation of pristine graphite oxide as room-temperature chemiresistive ammonia gas sensing material *Sensors* **17** 320
[9] Ma Y and Zhi L 2019 Graphene-based transparent conductive films: material systems, preparation and applications *Small Methods* **3** 1800199
[10] Li C, Zhang X, Sun C, Wang K, Sun X and Ma Y 2019 Recent progress of graphene-based materials in lithium-ion capacitors *J. Phys. D: Appl. Phys.* **52** 143001
[11] Choudhury A K R 2020 *Flame Retardants for Textile Materials* (Boca Raton, FL: CRC Press) (https://doi.org/10.1201/9780429032318)
[12] Laoutid F 2020 *Advanced Flame Retardant Materials* (Basel: MDPI) (https://doi.org/10.3390/books978-3-03928-351-4)
[13] de Wit C A 2002 An overview of brominated flame retardants in the environment *Chemosphere* **46** 583–624
[14] Levchik S V and Weil E D 2006 A review of recent progress in phosphorus-based flame retardants *J. Fire Sci.* **24** 345–64
[15] Kuriyama S N, Talsness C E, Grote K and Chahoud I 2005 Developmental exposure to low-dose PBDE-99: effects on male fertility and neurobehavior in rat offspring *Environ. Health Perspect.* **113** 149–54
[16] Schreder E D and La Guardia M J 2014 Flame retardant transfers from U.S. households (dust and laundry wastewater) to the aquatic environment *Environ. Sci. Technol.* **48** 11575–83
[17] Pantelaki I and Voutsa D 2019 Organophosphate flame retardants (OPFRs): a review on analytical methods and occurrence in wastewater and aquatic environment *Sci. Total Environ.* **649** 247–63
[18] Singh R K, Kumar R and Singh D P 2016 Graphene oxide: strategies for synthesis, reduction and frontier applications *RSC Adv.* **6** 64993–5011
[19] Wu W, Liu M, Gu Y, Guo B, Ma H, Wang P, Wang X and Zhang R 2020 Fast chemical exfoliation of graphite to few-layer graphene with high quality and large size via a two-step microwave-assisted process *Chem. Eng. J.* **381** 122592
[20] Xu Y, Cao H, Xue Y, Li B and Cai W 2018 Liquid-phase exfoliation of graphene: an overview on exfoliation media, techniques, and challenges *Nanomaterials* **8** 942
[21] Bannov A G, Jasek O, Manakhov A, Marik M, Necas D and Zajickova L 2017 High-performance ammonia gas sensors based on plasma treated carbon nanostructures *IEEE Sens. J.* **17** 1964–70
[22] Sun Y, Chen Z, Gong H, Li X, Gao Z, Xu S, Han X, Han B, Meng X and Zhang J 2020 Continuous 'Snowing' thermotherapeutic graphene *Adv. Mater.* **32** 2002024
[23] Sun Y, Yang L, Xia K, Liu H, Han D, Zhang Y and Zhang J 2018 'Snowing' graphene using microwave ovens *Adv. Mater.* **30** 1803189
[24] Dato A, Radmilovic V, Lee Z, Phillips J and Frenklach M 2008 Substrate-free gas-phase synthesis of graphene sheets *Nano Lett.* **8** 2012–6
[25] Tatarova E, Dias A, Henriques J, Do Rego A M B, Ferraria A M, Abrashev M V, Luhrs C C, Phillips J, Dias F M and Ferreira C M 2014 Microwave plasmas applied for the synthesis of free standing graphene sheets *J. Phys. D: Appl. Phys.* **47** 385501
[26] Tsyganov D *et al* 2016 On the plasma-based growth of 'flowing' graphene sheets at atmospheric pressure conditions *Plasma Sources Sci. Technol.* **25** 015013
[27] Zhong R and Hong R 2020 Continuous preparation and formation mechanism of few-layer graphene by gliding arc plasma *Chem. Eng. J.* **387** 124102
[28] Bom D, Andrews R, Jacques D, Anthony J, Chen B, Meier M S and Selegue J P 2002 Thermogravimetric analysis of the oxidation of multiwalled carbon nanotubes: evidence for the role of defect sites in carbon nanotube chemistry *Nano Lett.* **2** 615–9
[29] Crumpton D M, Laitinen R A, Smieja J and Cleary D A 1996 Thermal analysis of carbon allotropes: an experiment for advanced undergraduates *J. Chem. Educ.* **73** 590
[30] Chabot V, Kim B, Sloper B, Tzoganakis C and Yu A 2013 High yield production and purification of few layer graphene by Gum Arabic assisted physical sonication *Sci. Rep.* **3** 1378
[31] Toman J, Jasek O, Snirer M, Kudrle V and Jurmanova J 2019 On the interplay between plasma discharge instability and formation of free-standing graphene nanosheets in a dual-channel microwave plasma torch at atmospheric pressure *J. Phys. D: Appl. Phys.* **52** 265205
[32] Jašek O, Eliáš M, Zajíčková L, Kučerová Z, Matějková J, Rek A and Buršík J 2007 Discussion of important factors in deposition of carbon nanotubes by atmospheric pressure microwave plasma torch *J. Phys. Chem. Solids* **68** 738–43
[33] Limbu T B, Hernández J C, Mendoza F, Katiyar R K, Razink J J, Makarov V I, Weiner B R and Morell G 2018 A novel approach to the layer-number-controlled and grain-size-controlled growth of high quality graphene for nanoelectronics *ACS Appl. Nano Mater.* **1** 1502–12
[34] Yang G, Li L, Lee W B and Ng M C 2018 Structure of graphene and its disorders: a review *Sci. Technol. Adv. Mater.* **19** 613–48
[35] Liu Z, Suenaga K, Harris P J F and Iijima S 2009 Open and closed edges of graphene layers *Phys. Rev. Lett.* **102** 015501
[36] Dato A and Frenklach M 2010 Substrate-free microwave synthesis of graphene: experimental conditions and hydrocarbon precursors *New J. Phys.* **12** 125013
[37] Mu S-J, Su Y-C, Xiao L-H, Liu S-D, Hu T and Tang H-B 2013 X-ray diffraction pattern of graphite oxide *Chin. Phys. Lett.* **30** 096101
[38] Ferrari A C 2007 Raman spectroscopy of graphene and graphite: disorder, electron–phonon coupling, doping and nonadiabatic effects *Solid State Commun.* **143** 47–57
[39] Ferrari A C *et al* 2006 Raman spectrum of graphene and graphene layers *Phys. Rev. Lett.* **97** 187401
[40] Pimenta M A, Dresselhaus G, Dresselhaus M S, Cançado L G, Jorio A and Saito R 2007 Studying disorder in graphite-based systems by Raman spectroscopy *Phys. Chem. Chem. Phys.* **9** 1276–91
[41] Pawlyta M, Rouzaud J-N and Duber S 2015 Raman microspectroscopy characterization of carbon blacks: spectral analysis and structural information *Carbon* **84** 479–90
[42] Sadezky A, Muckenhuber H, Grothe H, Niessner R and Pöschl U 2005 Raman microspectroscopy of soot and related carbonaceous materials: spectral analysis and structural information *Carbon* **43** 1731–42
[43] May P, Lazzeri M, Venezuela P, Herziger F, Callsen G, Reparaz J S, Hoffmann A, Mauri F and Maultzsch J 2013 Signature of the two-dimensional phonon dispersion in graphene probed by double-resonant Raman scattering *Phys. Rev.* B **87** 075402
[44] Kaniyoor A and Ramaprabhu S 2012 A Raman spectroscopic investigation of graphite oxide derived grapheme *AIP Adv.* **2** 032183
[45] Cançado L G, da Silva M G, Martins Ferreira E H, Hof F, Kampioti K, Huang K, Pénicaud A, Achete C A, Capaz R B and Jorio A 2017 Disentangling contributions of point and

line defects in the Raman spectra of graphene-related materials *2D Mater.* **4** 025039
[46] Gupta A K, Russin T J, Gutiérrez H R and Eklund P C 2009 Probing graphene edges via Raman scattering *ACS Nano* **3** 45–52
[47] Rybachuk M and Bell J M 2009 Electronic states of trans-polyacetylene, poly(p-phenylene vinylene) and sp-hybridised carbon species in amorphous hydrogenated carbon probed by resonant Raman scattering *Carbon* **47** 2481–90
[48] Barinov A, Bariş Malcioğlu O, Fabris S, Sun T, Gregoratti L, Dalmiglio M and Kiskinova M 2009 Initial stages of oxidation on graphitic surfaces: photoemission study and density functional theory calculations *J. Phys. Chem.* C **113** 9009–13
[49] Ganesan K, Ghosh S, Gopala Krishna N, Ilango S, Kamruddin M and Tyagi A K 2016 A comparative study on defect estimation using XPS and Raman spectroscopy in few layer nanographitic structures *Phys. Chem. Chem. Phys.* **18** 22160–7
[50] Blume R, Rosenthal D, Tessonnier J-P, Li H, Knop-Gericke A and Schlögl R 2015 Characterizing graphitic carbon with x-ray photoelectron spectroscopy: a step-by-step approach *ChemCatChem* **7** 2871–81
[51] Doniach S and Sunjic M 1970 Many-electron singularity in x-ray photoemission and x-ray line spectra from metals *J. Phys. C: Solid State Phys.* **3** 285–91
[52] Morgan P A, Robertson S D and Unsworth J F 1986 Combustion studies by thermogravimetric analysis *Fuel* **65** 1546–51
[53] Yan J, Wang Q, Wei T, Jiang L, Zhang M, Jing X and Fan Z 2014 Template-assisted low temperature synthesis of functionalized graphene for ultrahigh volumetric performance supercapacitors *ACS Nano* **8** 4720–9
[54] Li Z, Zhang J, Li Y, Guan Y, Feng Z and Li C 2006 Preparation and characterization of ordered mesoporous carbons on SBA-15 template *J. Mater. Chem.* **16** 1350
[55] Van T D N, Sufian S, Mansor N and Yahya N 2014 Characterization of carbon nanofibers treated with thermal nitrogen as a catalyst support using point-of-zero charge analysis *J. Nanomater.* **2014** 1–6
[56] Ghosh S, Polaki S R, Ajikumar P K, Krishna N G and Kamruddin M 2018 Aging effects on vertical graphene nanosheets and their thermal stability *Indian J. Phys.* **92** 337–42
[57] Melero C, Rincón R, Muñoz J, Zhang G, Sun S, Perez A, Royuela O, González-Gago C and Calzada M D 2018 Scalable graphene production from ethanol decomposition by microwave argon plasma torch *Plasma Phys. Control. Fusion* **60** 014009
[58] Fronczak M, Fazekas P, Károly Z, Hamankiewicz B and Bystrzejewski M 2017 Continuous and catalyst free synthesis of graphene sheets in thermal plasma jet *Chem. Eng. J.* **322** 385–96
[59] Wu X, Liu Y, Yang H and Shi Z 2016 Large-scale synthesis of high-quality graphene sheets by an improved alternating current arc-discharge method *RSC Adv.* **6** 93119–24
[60] Amirov R, Shavelkina M, Alihanov N, Shkolnikov E, Tyuftyaev A and Vorob'eva N 2015 Direct synthesis of porous multilayer graphene materials using thermal plasma at low pressure *J. Nanomater.* **2015** 1–6
[61] Achee T C, Sun W, Hope J T, Quitzau S G, Sweeney C B, Shah S A, Habib T and Green M J 2018 High-yield scalable graphene nanosheet production from compressed graphite using electrochemical exfoliation *Sci. Rep.* **8** 14525
[62] Park K H, Kim B H, Song S H, Kwon J, Kong B S, Kang K and Jeon S 2012 Exfoliation of non-oxidized graphene flakes for scalable conductive film *Nano Lett.* **12** 2871–6
[63] Greco E, Nava G, Fathi R, Fumagalli F, Del Rio-Castillo A E, Ansaldo A, Monaco S, Bonaccorso F, Pellegrini V and Di Fonzo F 2017 Few-layer graphene improves silicon performance in Li-ion battery anodes *J. Mater. Chem.* A **5** 19306–15
[64] Shanov V, Cho W, Malik R, Alvarez N, Haase M, Ruff B, Kienzle N, Ochmann T, Mast D and Schulz M 2013 CVD growth, characterization and applications of carbon nanostructured materials *Surf. Coat. Technol.* **230** 77–86
[65] Fraser R D B and Suzuki E 1969 Resolution of overlapping bands. Functions for simulating band shapes *Anal. Chem.* **41** 37–39
[66] Bannov A G, Manakhov A, Shibaev A A, Ukhina A V, Polčák J and Maksimovskii E A 2018 Synthesis dynamics of graphite oxide *Thermochim. Acta* **663** 165–75
[67] Tang J, Song Q, He B and Yao Q 2009 Oxidation behavior of a kind of carbon black *Sci. China* E **52** 1535–42
[68] Bannov A G, Timofeeva A A, Shinkarev V V, Dyukova K D, Ukhina A V, Maksimovskii E A and Yusin S I 2014 Synthesis and studies of properties of graphite oxide and thermally expanded graphite *Prot. Met. Phys. Chem. Surf.* **50** 183–90
[69] Demidov A I and Markelov I A 2005 Thermodynamics of reaction of carbon with oxygen *Russ. J. Appl. Chem.* **78** 707–10
[70] Van Khai T *et al* 2013 Direct production of highly conductive graphene with a low oxygen content by a microwave-assisted solvothermal method *Chem. Eng. J.* **232** 346–55
[71] Munuera J M, Paredes J I, Villar-Rodil S, Ayán-Varela M, Pagán A, Aznar-Cervantes S D, Cenis J L, Martínez-Alonso A and Tascón J M D 2015 High quality, low oxygen content and biocompatible graphene nanosheets obtained by anodic exfoliation of different graphite types *Carbon* **94** 729–39
[72] Bagri A, Mattevi C, Acik M, Chabal Y J, Chhowalla M and Shenoy V B 2010 Structural evolution during the reduction of chemically derived graphene oxide *Nat. Chem.* **2** 581–7
[73] Figueiredo J L and Pereira M F R 2010 The role of surface chemistry in catalysis with carbons *Catal. Today* **150** 2–7
[74] Liu W and Zhang W 2018 Oxygen annealing induced defect generation in monolayer and bilayer graphene *Nano Adv.* **3** 6–11
[75] Bagchi S, Johnson H T and Chew H B 2020 Rotational stability of twisted bilayer grapheme *Phys. Rev.* B **101** 054109
[76] Dato A, Lee Z, Jeon K-J, Erni R, Radmilovic V, Richardson T J and Frenklach M 2009 Clean and highly ordered graphene synthesized in the gas phase *Chem. Commun.* **40** 6095–7
[77] Ferreira H, Poma G, Acosta D R, Barzola-Quiquia J, Quintana M, Barreto L and Champi A 2018 Laser power influence on Raman spectra of multilayer graphene, multilayer graphene oxide and reduced multilayer graphene oxide *J. Phys.: Conf. Ser.* **1143** 012020
[78] Calizo I, Balandin A A, Bao W, Miao F and Lau C N 2007 Temperature dependence of the Raman spectra of graphene and graphene multilayers *Nano Lett.* **7** 2645–9
[79] Venezuela P, Lazzeri M and Mauri F 2011 Theory of double-resonant Raman spectra in graphene: intensity and line shape of defect-induced and two-phonon bands *Phys. Rev.* B **84** 035433